Pressure-Based Adaption Indicator for Compressible Euler Equations

Jeremy Dewar,[1] **Alexander Kurganov,**[1] **Maren Leopold**[2]
[1] *Mathematics Department, Tulane University, New Orleans, Louisiana 70118*

[2] *Chevron, Houston, Texas 77002*

Received 18 February 2014; accepted 12 January 2015
Published online 18 February 2015 in Wiley Online Library (wileyonlinelibrary.com).
DOI 10.1002/num.21970

We consider the Euler equations of gas dynamics and develop a new adaption indicator, which is based on the weak local residual measured for the nonconservative pressure variable. We demonstrate that the proposed indicator is capable of automatically detecting discontinuities and distinguishing between the shock and contact waves when they are isolated from each other. We then use the developed indicator to design a scheme adaption algorithm, according to which nonlinear limiters are used only in the vicinity of shocks. The new adaption algorithm is realized using a second-order limited and a high-order nonlimited central-upwind scheme. We demonstrate robustness and high resolution of the designed method on a number of one- and two-dimensional numerical examples. Numer Methods Partial Differential Eq 31: 1844–1874, 2015

Keywords: adaption indicator; Euler equations of gas dynamics; finite-volume methods; scheme adaption algorithm; weak local residual

I. INTRODUCTION

This article describes a new scheme adaption algorithm for the Euler equations of gas dynamics, which in the one-dimensional (1-D) case read as

$$\begin{cases} \rho_t + (\rho u)_x = 0, \\ (\rho u)_t + (\rho u^2 + p)_x = 0, \\ E_t + (u(E+p))_x = 0, \end{cases} \tag{1.1}$$

where ρ is the density, u is the velocity, ρu is the momentum, E is the total energy and p is the pressure. The system (1.1) is closed through the equation of state, which for ideal gases (with the

Correspondence to: Alexander Kurganov, Mathematics Department, Tulane University, New Orleans, LA 70118 (e-mail: kurganov@math.tulane.edu)
Contract grant sponsor: NSF; contract grant number: DMS-1115718 (A.K.)
Contract grant sponsor: LONI institute (LI), under the Louisiana Board of Regents; contract grant number: LEQSF(2007-12)-ENH-PKSFI-PRS-0 (J.D.)
Contract grant sponsor: NSF Grant; contract grant number: DMS-0610430 (J.D., A.K., and M.L.)

heat capacity ratio defined as γ) is given by

$$E = \frac{p}{\gamma - 1} + \frac{\rho u^2}{2}. \tag{1.2}$$

The system (1.1), (1.2) is a hyperbolic system of conservation laws, which as it is well-known admits discontinuous solutions, and when numerically solved using a method which is only linearly stable, the approximate solution may develop strong nonphysical oscillations and even blow up.

We focus on Godunov-type finite-volume methods, which belong to the class of projection-evolution methods. The computed solution, realized in terms of its cell averages is first projected into the space of piecewise polynomials and then evolved to the next time level according to the integral form of the studied system of conservation laws, which in the general case can be written in the following vector form:

$$\boldsymbol{q}_t + \boldsymbol{f}(\boldsymbol{q})_x = \boldsymbol{0},$$

where $\boldsymbol{q}(x,t)$ is a vector of unknowns and $\boldsymbol{f}(\boldsymbol{q}(x,t))$ is a flux function.

For the sake of simplicity we will consider only uniform meshes with $x_\mu = \mu \Delta x$. Assume that at a certain time level t the computed cell averages,

$$\overline{\boldsymbol{q}}_j(t) :\approx \int_{I_j} \boldsymbol{q}(x,t)dx, \quad I_j := \left(x_{j-\frac{1}{2}}, x_{j+\frac{1}{2}}\right),$$

are available. They are then used to build a piecewise polynomial reconstruction

$$\tilde{\boldsymbol{q}}(x;t) = \sum_j \chi_{I_j} \mathcal{P}_j(x;t), \tag{1.3}$$

where χ is a characteristic function and $\mathcal{P}_j$ are polynomials in x of a certain degree.

To construct a stable finite-volume method, the polynomials $\mathcal{P}_j$ should be sufficiently accurate and nonoscillatory. The latter is typically enforced via a nonlinear limiter used in the computation of its derivatives. This is done in an attempt to prevent the appearance of large spurious oscillations in the nonsmooth parts of the solution.

The (formal) order of the method will be determined by the (formal) order of accuracy of the piecewise polynomial reconstruction (1.3). To obtain a second-order method one needs to use a piecewise linear reconstruction

$$\tilde{\boldsymbol{q}}(x;t) = \overline{\boldsymbol{q}}_j(t) + \left(\boldsymbol{q}_x\right)_j(t)(x - x_j), \quad x_{j-\frac{1}{2}} < x < x_{j+\frac{1}{2}}. \tag{1.4}$$

There is a library of reliable limiters for computing $(\boldsymbol{q}_x)_j$ (see, e.g., [1–6]). To achieve higher than second order accuracy, higher degree polynomials have to be used in (1.3). High-order limited reconstructions have been extensively studied (see, e.g., [7–9]), but their major drawback is a very high computational cost. They may also cause the resolution of smooth parts of the computed solution to deteriorate. This leads to the idea of scheme adaption: Detect nonsmooth parts of the computed solution and only in those portions of the computational domain apply nonlinear limiters. Adaptive approaches are thus based on the indicators used to detect the "rough" parts of the computed solutions.

Adaption indicators aim to detect discontinuities in the solution and many indicators have been proposed and studied. In [10, 11], discontinuities are detected using Richardson-type estimates of the local truncation error of the solution. However, this error estimation procedure assumes smoothness of the solution and ceases to be valid near discontinuities. A more heuristic approach is examined in [12–14] where the local wave strengths of the upwind scheme are used as a measure of solution smoothness. In [15–18], the multiresolution coefficients of the wavelets expansion are used. In [19–22], the edges in the computed solution were detected using its Fourier coefficient. In [23–25], the "rough" parts of the computed solution were identified using the numerical production of entropy, while the same goal was achieved in [26, 27] using the entropy residual.

Most of the existing adaption/smoothness indicators rely on data analysis, which may not take into account the quality of the computed solution. This may cause, for example, redundant adaptive mesh refinement in the vicinities of accurately resolved discontinuous waves or, on the contrary, may lead to an automatic assumption that any smooth part of the solution is accurately captured, which may not be true. The indicator proposed in [28] was designed to measure the weak local residuals (WLR) and by this the quality of the computed solution is automatically taken into account in the scheme and mesh adaption strategies developed in [29, 30]. The main idea in [28] was to substitute the computed solution into the weak formulation of the conservation law and to approximate the global test function with the help of the localized quadratic B-splines. This allows one to write the weak residual as a linear combination of WLRs, which themselves can be used as a tool to measure the local quality of the solution.

In [28], it has been demonstrated that in the 1-D case, the WLR-based indicator is $\mathcal{O}(\Delta x)$ near shocks and $\mathcal{O}((\Delta x)^{\delta}), 1 < \delta < 2$, near contact waves, while it is much smaller in smooth areas, $\mathcal{O}((\Delta x)^{\min(r+2,5)})$, where r is the (formal) order of the underlying scheme. This suggests a straightforward scheme adaption strategy implemented in [30]: If the WLR is above a certain threshold it is assumed that the local area is in the vicinity of a discontinuity and a limiter has to be used to prevent oscillations, while if the value of the WLR is below the threshold, the computed solution is assumed to be locally smooth and a higher-order, nonlimited method may be safely applied there.

In [29], the above adaption strategy was refined in an attempt to distinguish between the shock and contact discontinuities. However, the main drawback of the adaptive strategy in [29] is the lack of robustness in the detection of shocks. Even though the values of the indicator used in [30] (or its simpler version used in [19]) at shocks and at contacts are typically different, finding the correct threshold is not easy and the selection of the adaptive constant requires nonrobust, problem-oriented tuning.

In this article, we propose a new adaption indicator (AI). Our AI uses one of the main features of contact waves—the thermal pressure and velocity are continuous across them, while both quantities jump across shocks. In the construction of our pressure-based AI, we chose to measure the WLR for the pressure equation, which in the 1-D case reads

$$p_t + (pu)_x = -(\gamma - 1)pu_x. \tag{1.5}$$

To this end, we substitute the computed solution into the following integral formulation of (1.5):

$$\int_{\mathbb{R}} \{p\Phi_t + (pu)\Phi_x - (\gamma - 1)pu_x\Phi\}\, dxdt = 0, \tag{1.6}$$

where the test function $\Phi \in C_0^1(\mathbb{R})$. As in [28–30], we replace the global test function Φ with the B-splines and obtain the pressure-based AI. We demonstrate that the values of the proposed AI are

practically as small in the vicinity of isolated contact waves as in the continuous regions, while in the neighborhoods of shocks their values are still $\mathcal{O}(\Delta x)$. We then use this fact to automatically detect the positions of shock waves.

Note that we do *not* use the nonconservative Eq. (1.5) to evolve the pressure—we only use (1.5) for measuring the WLR for the numerical solution obtained by a conservative numerical method. We therefore do not expect to encounter any of the problems one typically has to face while working with nonconservative methods, see, for example, [31].

We implement the proposed scheme adaption strategy using the pressure-based AI as follows: We detect shock areas and only in those areas use a second-order limited reconstruction, while elsewhere in the domain a higher-order nonlimited reconstruction is utilized. Our scheme adaption method is realized using a semidiscrete Godunov-type central-upwind scheme, which is a simple, robust and universal Riemann-problem-solver-free method for general systems of conservation laws, see [32–35]. We would like to emphasize, however, that our adaption strategy is not tied to the specific choice of a central-upwind scheme; one can use one's favorite Godunov-type method instead.

The article is organized as follows. In Section II, we describe our pressure-based AI for 1-D and 2-D problems. In Section III, we detail our particular adaption algorithm using the pressure-based AI. Finally, in Section IV, we numerically study the rates of decay of the new AI and demonstrate the performance of the proposed scheme adaption method on a number of both 1-D and 2-D numerical examples.

II. NEW PRESSURE-BASED ADAPTION INDICATOR

In our scheme adaption method, we will use the WLR as an indicator of "rough" parts of a computed solution. In this section, we describe the new pressure-based AI used in our algorithm. This AI is a modified version of the indicators from [28–30].

A. One-Dimensional Adaption Indicator

Consider a general hyperbolic equation of the form

$$q_t + f(q)_x = S, \tag{2.1}$$

where $S(q,x,t)$ is a source term. By definition, a weak solution $q(x, t)$ of (2.1) satisfies the integral identity

$$\begin{aligned} E(q,\Phi) := &\int_{\mathbb{R}}\int_0^\infty \{q(x,t)\Phi_t(x,t) + f(q(x,t))\Phi_x(x,t) + S(q,x,t)\Phi(x,t)\}\,dxdt \\ &+ \int_{\mathbb{R}} q(x,0)\Phi(x,0)dx = 0, \end{aligned} \tag{2.2}$$

for all smooth compactly supported test functions Φ. The key idea in [28] was to develop an indicator that checks by how much the computed solution, denoted by q^Δ, fails to satisfy equation (2.2), that is, to measure a weak residual. Following [28–30], we take q^Δ to be the corresponding piecewise constant approximation defined by

$$q^\Delta(x,t) := q^n_{j+\frac{1}{2}} \quad \text{if } (x,t) \in [x_j, x_{j+1}) \times [t^{n-\frac{1}{2}}, t^{n+\frac{1}{2}}), \tag{2.3}$$

where $q^n_{j+\frac{1}{2}}$ is a point value of the solution computed at $x = x_{j+\frac{1}{2}}$ and $t = t^n$.

To measure the quality of the computed solution, we would like to evaluate $E(q^{\Delta}, \Phi)$. To this end, we approximate a general smooth test function Φ with a set of test functions $\Phi^{n-\frac{1}{2}}_{j+\frac{1}{2}}$ localized around $\left(x_{j+\frac{1}{2}}, t^{n-\frac{1}{2}}\right)$ such that

$$\Phi(x,t) = \sum_{j,n} c^{n-\frac{1}{2}}_{j+\frac{1}{2}} \Phi^{n-\frac{1}{2}}_{j+\frac{1}{2}}(x,t) + \mathcal{O}((\Delta x)^{\ell_1} + (\Delta t)^{\ell_2}),$$

where ℓ_1 and ℓ_2 are the orders of the spatial and temporal approximations, respectively. We then may define $E^{n-\frac{1}{2}}_{j+\frac{1}{2}} := E\left(q^{\Delta}, \Phi^{n-\frac{1}{2}}_{j+\frac{1}{2}}\right)$, which will be referred to as the WLR, and obtain

$$E(q^{\Delta}, \Phi) = \sum_{j,n} c^{n-\frac{1}{2}}_{j+\frac{1}{2}} E^{n-\frac{1}{2}}_{j+\frac{1}{2}} + \mathcal{O}(\Delta^m), \tag{2.4}$$

where $\Delta = \max(\Delta x, \Delta t)$ and $m = \min(\ell_1, \ell_2)$. The WLR—as it was demonstrated in [28, 30]—can be used as an indicator of "rough" solution regions.

Similar to [28–30] we make the particular choice of $\Phi^{n-\frac{1}{2}}_{j+\frac{1}{2}}$ to be a product of two localized B-splines. However, this time, we choose $B_{j+\frac{1}{2}}(x)$ to be quadratic and $B^{n-\frac{1}{2}}(t)$ to be linear, with supports of size $3\Delta x$ and $2\Delta t$, respectively:

$$\Phi^{n-\frac{1}{2}}_{j+\frac{1}{2}}(x,t) = B^{n-\frac{1}{2}}(t) B_{j+\frac{1}{2}}(x), \tag{2.5}$$

where

$$B^{n-\frac{1}{2}}(t) := \begin{cases} \frac{t^{n+\frac{1}{2}} - t}{\Delta t}, & t^{n-\frac{1}{2}} \le t \le t^{n+\frac{1}{2}}, \\ \frac{t - t^{n-\frac{3}{2}}}{\Delta t}, & t^{n-\frac{3}{2}} \le t \le t^{n-\frac{1}{2}}, \end{cases} \tag{2.6}$$

$$B_{j+\frac{1}{2}}(x) := \begin{cases} \left(\frac{x - x_{j-1}}{\Delta x}\right)^2, & x_{j-1} \le x \le x_j, \\ \frac{3}{4} - \left(\frac{x - x_{j+\frac{1}{2}}}{\Delta x}\right)^2, & x_j \le x \le x_{j+1}, \\ \left(\frac{x - x_{j+2}}{\Delta x}\right)^2, & x_{j+1} \le x \le x_{j+2}. \end{cases} \tag{2.7}$$

Note that the splines $\left\{\Phi^{n-\frac{1}{2}}_{j+\frac{1}{2}}\right\}$ satisfy the approximation property (2.4) with $m = 2$.

Remark 2.1. In contrast to [28, 30], we choose $B^{n-\frac{1}{2}}(t)$ to be a linear B-spline rather than a quadratic one. The resulting expression for our AI is thus substantially simplified as one no longer needs to use the computed solutions from three consecutive time levels. This makes the proposed adaption strategy more flexible. At the same time, the temporal accuracy of the new AI is not as high as of the indicator used in [28, 30].

When applied to the Euler equations of gas dynamics one can base an AI on the WLR of any of the equations in (1.1). However, by doing this it will be hard to design a method capable of

distinguishing between shock and contact waves since all of the conservative variables—ρ,ρu and E—jump across both shocks and contacts. We therefore base our AI on the nonconservative quantity of pressure which satisfies (1.5) and jumps across shocks while staying continuous at contact waves. To this end, we write the integral version of the pressure equation (1.5) by treating the term on its right-hand side (RHS), - $(\gamma-1)pu_x$, as the source S appearing on the RHS of (2.1):

$$\int_{\mathbb{R}}\int_0^{\infty}\{p\Phi_t + pu\Phi_x - (\gamma-1)pu_x\Phi\}dxdt + \int_{\mathbb{R}} p(x,0)\Phi(x,0)dx = 0.$$

Using this integral formulation of the pressure equation, we define the pressure-based WLRs as

$$E^{n-\frac{1}{2}}_{j+\frac{1}{2}} := E\left(p^{\Delta}, u^{\Delta}, u_x^{\Delta}, \Phi^{n-\frac{1}{2}}_{j+\frac{1}{2}}\right) = \int_{t^{n-\frac{3}{2}}}^{t^{n+\frac{1}{2}}}\int_{x_{j-1}}^{x_{j+2}}\left\{p^{\Delta}\left(\Phi^{n-\frac{1}{2}}_{j+\frac{1}{2}}\right)_t + p^{\Delta}u^{\Delta}\left(\Phi^{n-\frac{1}{2}}_{j+\frac{1}{2}}\right)_x - (\gamma-1)p^{\Delta}u_x^{\Delta}\Phi^{n-\frac{1}{2}}_{j+\frac{1}{2}}\right\}dxdt. \tag{2.8}$$

where p^{Δ}, u^{Δ} and u_x^{Δ} are piecewise constant approximations of the computed p, u and u_x, respectively. These approximations are defined the same way as q^{Δ} was defined in (2.3).

Using (2.3) and (2.5), we compute the integral on the RHS of (2.8) and arrive at the following formula for the pressure-based AI:

$$\begin{aligned}E^{n-\frac{1}{2}}_{j+\frac{1}{2}} = {}& \frac{\Delta x}{6}\left[p^n_{j-\frac{1}{2}} - p^{n-1}_{j-\frac{1}{2}} + 4\left(p^n_{j+\frac{1}{2}} - p^{n-1}_{j+\frac{1}{2}}\right) + p^n_{j+\frac{3}{2}} - p^{n-1}_{j+\frac{3}{2}}\right]\\ &+ \frac{\Delta t}{4}\left[p^n_{j+\frac{3}{2}}u^n_{j+\frac{3}{2}} - p^n_{j-\frac{1}{2}}u^n_{j-\frac{1}{2}} + p^{n-1}_{j+\frac{3}{2}}u^{n-1}_{j+\frac{3}{2}} - p^{n-1}_{j-\frac{1}{2}}u^{n-1}_{j-\frac{1}{2}}\right]\\ &+ \frac{\Delta x\Delta t}{12}(\gamma-1)\left[p^n_{j-\frac{1}{2}}(u_x)^n_{j-\frac{1}{2}} + p^{n-1}_{j-\frac{1}{2}}(u_x)^{n-1}_{j-\frac{1}{2}} + 4\left(p^n_{j+\frac{1}{2}}(u_x)^n_{j+\frac{1}{2}} + p^{n-1}_{j+\frac{1}{2}}(u_x)^{n-1}_{j+\frac{1}{2}}\right) + p^n_{j+\frac{3}{2}}(u_x)^n_{j+\frac{3}{2}} + p^{n-1}_{j+\frac{3}{2}}(u_x)^{n-1}_{j+\frac{3}{2}}\right].\end{aligned} \tag{2.9}$$

To be able to use (2.9) in practice, we need to compute the point values of u_x in terms of the reconstructed point values of the conservative quantities ρ and ρu. For example, one can use a simple second-order central difference to obtain

$$(u_x)^n_{j+\frac{1}{2}} := \frac{u^n_{j+\frac{3}{2}} - u^n_{j-\frac{1}{2}}}{2\Delta x} = \frac{1}{2\Delta x}\left(\frac{(\rho u)^n_{j+\frac{3}{2}}}{\rho^n_{j+\frac{3}{2}}} - \frac{(\rho u)^n_{j-\frac{1}{2}}}{\rho^n_{j-\frac{1}{2}}}\right). \tag{2.10}$$

B. Two-Dimensional Adaption Indicator

In this section, we extend the pressure-based AI to the 2-D compressible Euler equations,

$$\begin{cases} \rho_t + (\rho u)_x + (\rho v)_y = 0, \\ (\rho u)_t + (\rho u^2 + p)_x + (\rho uv)_y = 0, \\ (\rho v)_t + (\rho uv)_x + (\rho v^2 + p)_y = 0, \\ E_t + (u(E+p))_x + (v(E+p))_y = 0, \end{cases} \tag{2.11}$$

where ρ, E and p are, as in the 1-D case, the density, total energy and pressure, respectively, ρu is the x-momentum, and ρv is the y-momentum. The system (2.11) is closed through the equation of state,

$$E = \frac{p}{\gamma - 1} + \frac{\rho(u^2 + v^2)}{2}. \tag{2.12}$$

As in [30], the 2-D extension of the 1-D AI is rather straightforward. Our localized test-functions are now defined as

$$\Phi^{n-\frac{1}{2}}_{j+\frac{1}{2},k+\frac{1}{2}}(x,y,t) := B^{n-\frac{1}{2}}(t) B_{j+\frac{1}{2}}(x) B_{k+\frac{1}{2}}(y), \tag{2.13}$$

where $B^{n-\frac{1}{2}}(t)$ and $B_{j+\frac{1}{2}}(x)$ are given by (2.6) and (2.7), and

$$B_{k+\frac{1}{2}}(y) := \begin{cases} \left(\dfrac{y - y_{k-1}}{\Delta y}\right)^2, & y_{k-1} \le y \le y_k, \\ \dfrac{3}{4} - \left(\dfrac{y - y_{k+\frac{1}{2}}}{\Delta y}\right)^2, & y_k \le y \le y_{k+1}, \\ \left(\dfrac{y - y_{k+2}}{\Delta y}\right)^2, & y_{k+1} \le y \le y_{k+2}, \end{cases} \tag{2.14}$$

where Δy is the mesh size in the y-direction and $y_\nu = \nu \Delta y$. We now take the 2-D pressure equation,

$$p_t + (pu)_x + (pv)_y = -(\gamma - 1) p (u_x + v_y), \tag{2.15}$$

and as in the 1-D case rewrite it in the integral form:

$$\int_{\mathbb{R}^2} \int_0^\infty \{p\Phi_t + pu\Phi_x + pv\Phi_y - (\gamma - 1)p(u_x + v_y)\Phi\} dxdydt + \int_{\mathbb{R}} p(x,y,0)\Phi(x,y,0) dxdy = 0.$$

We then substitute the piecewise constant approximation of the computed solution (in the 2-D case, it is obtained similarly to the 1-D approximation given in (2.3)) together with the localized

test functions (2.13) into the left-hand side of (2.15), evaluate the obtained integrals, and arrive at the following formula for the 2-D pressure-based AI:

$$
\begin{aligned}
E^{n-\frac{1}{2}}_{j+\frac{1}{2},k+\frac{1}{2}} &:= E(p^{\Delta}, u^{\Delta}, v^{\Delta}, u^{\Delta}_{x}, v^{\Delta}_{y}, \Phi^{n-\frac{1}{2}}_{j+\frac{1}{2},k+\frac{1}{2}}) = \\
&\frac{\Delta x \Delta y}{36}\left[p^{n}_{j-\frac{1}{2},k-\frac{1}{2}} - p^{n-1}_{j-\frac{1}{2},k-\frac{1}{2}} + 4\left(p^{n}_{j-\frac{1}{2},k+\frac{1}{2}} - p^{n-1}_{j-\frac{1}{2},k+\frac{1}{2}}\right) + p^{n}_{j-\frac{1}{2},k+\frac{3}{2}} - p^{n-1}_{j-\frac{1}{2},k+\frac{3}{2}}\right. \\
&\quad +4\left(p^{n}_{j+\frac{1}{2},k-\frac{1}{2}} - p^{n-1}_{j+\frac{1}{2},k-\frac{1}{2}} + 4\left(p^{n}_{j+\frac{1}{2},k+\frac{1}{2}} - p^{n-1}_{j+\frac{1}{2},k+\frac{1}{2}}\right) + p^{n}_{j+\frac{1}{2},k+\frac{3}{2}} - p^{n-1}_{j+\frac{1}{2},k+\frac{3}{2}}\right) \\
&\quad \left.+p^{n}_{j+\frac{3}{2},k-\frac{1}{2}} - p^{n-1}_{j+\frac{3}{2},k-\frac{1}{2}} + 4\left(p^{n}_{j+\frac{3}{2},k+\frac{1}{2}} - p^{n-1}_{j+\frac{3}{2},k+\frac{1}{2}}\right) + p^{n}_{j+\frac{3}{2},k+\frac{3}{2}} - p^{n-1}_{j+\frac{3}{2},k+\frac{3}{2}}\right] \\
&+\frac{\Delta y \Delta t}{24}\left[(pu)^{n}_{j+\frac{3}{2},k-\frac{1}{2}} - (pu)^{n}_{j-\frac{1}{2},k-\frac{1}{2}} + (pu)^{n-1}_{j+\frac{3}{2},k-\frac{1}{2}} - (pu)^{n-1}_{j-\frac{1}{2},k-\frac{1}{2}}\right. \\
&\quad +4\left((pu)^{n}_{j+\frac{3}{2},k+\frac{1}{2}} - (pu)^{n}_{j-\frac{1}{2},k+\frac{1}{2}} + (pu)^{n-1}_{j+\frac{3}{2},k+\frac{1}{2}} - (pu)^{n-1}_{j-\frac{1}{2},k+\frac{1}{2}}\right) \\
&\quad \left.+(pu)^{n}_{j+\frac{3}{2},k+\frac{3}{2}} - (pu)^{n}_{j-\frac{1}{2},k+\frac{3}{2}} + (pu)^{n-1}_{j+\frac{3}{2},k+\frac{3}{2}} - (pu)^{n-1}_{j-\frac{1}{2},k+\frac{3}{2}}\right] \\
&+\frac{\Delta x \Delta t}{24}\left[(pv)^{n}_{j-\frac{1}{2},k+\frac{3}{2}} - (pv)^{n}_{j-\frac{1}{2},k-\frac{1}{2}} + (pv)^{n-1}_{j-\frac{1}{2},k+\frac{3}{2}} - (pv)^{n-1}_{j-\frac{1}{2},k-\frac{1}{2}}\right. \\
&\quad +4\left((pv)^{n}_{j+\frac{1}{2},k+\frac{3}{2}} - (pv)^{n}_{j+\frac{1}{2},k-\frac{1}{2}} + (pv)^{n-1}_{j+\frac{1}{2},k+\frac{3}{2}} - (pv)^{n-1}_{j+\frac{1}{2},k-\frac{1}{2}}\right) \\
&\quad \left.+(pv)^{n}_{j+\frac{3}{2},k+\frac{3}{2}} - (pv)^{n}_{j+\frac{3}{2},k-\frac{1}{2}} + (pv)^{n-1}_{j+\frac{3}{2},k+\frac{3}{2}} - (pv)^{n-1}_{j+\frac{3}{2},k-\frac{1}{2}}\right] \\
&+\frac{\Delta x \Delta y \Delta t}{72}(\gamma-1)\left[(p(u_x+v_y))^{n}_{j+\frac{3}{2},k-\frac{1}{2}} + 4(p(u_x+v_y))^{n}_{j+\frac{3}{2},k+\frac{1}{2}} + (p(u_x+v_y))^{n}_{j+\frac{3}{2},k+\frac{3}{2}}\right. \\
&\quad +4\left((p(u_x+v_y))^{n}_{j+\frac{1}{2},k-\frac{1}{2}} + 4(p(u_x+v_y))^{n}_{j+\frac{1}{2},k+\frac{1}{2}} + (p(u_x+v_y))^{n}_{j+\frac{1}{2},k+\frac{3}{2}}\right) \\
&\quad +(p(u_x+v_y))^{n}_{j-\frac{1}{2},k-\frac{1}{2}} + 4(p(u_x+v_y))^{n}_{j-\frac{1}{2},k+\frac{1}{2}} + (p(u_x+v_y))^{n}_{j-\frac{1}{2},k+\frac{3}{2}} \\
&\quad +(p(u_x+v_y))^{n-1}_{j+\frac{3}{2},k-\frac{1}{2}} + 4(p(u_x+v_y))^{n-1}_{j+\frac{3}{2},k+\frac{1}{2}} + (p(u_x+v_y))^{n-1}_{j+\frac{3}{2},k+\frac{3}{2}} \\
&\quad +4\left((p(u_x+v_y))^{n-1}_{j+\frac{1}{2},k-\frac{1}{2}} + 4(p(u_x+v_y))^{n-1}_{j+\frac{1}{2},k+\frac{1}{2}} + (p(u_x+v_y))^{n-1}_{j+\frac{1}{2},k+\frac{3}{2}}\right) \\
&\quad \left.+(p(u_x+v_y))^{n-1}_{j-\frac{1}{2},k-\frac{1}{2}} + 4(p(u_x+v_y))^{n-1}_{j-\frac{1}{2},k+\frac{1}{2}} + (p(u_x+v_y))^{n-1}_{j-\frac{1}{2},k+\frac{3}{2}}\right].
\end{aligned}
\tag{2.16}
$$

For the sake of brevity in (2.16), we have used the following shorthand notation:

$$
(p(u_x+v_y))^{n}_{j+\frac{1}{2},k+\frac{1}{2}} := p^{n}_{j+\frac{1}{2},k+\frac{1}{2}}\left((u_x)^{n}_{j+\frac{1}{2},k+\frac{1}{2}} + (v_y)^{n}_{j+\frac{1}{2},k+\frac{1}{2}}\right).
$$

To be able to use (2.16) in an adaption algorithm, we will need to compute the point values of u_x and v_y. As in (2.10), this is done using the reconstructed point values of the corresponding conservative quantities. For example, the second-order central difference gives

$$(u_x)^n_{j+\frac{1}{2},k+\frac{1}{2}} := \frac{u^n_{j+\frac{3}{2},k+\frac{1}{2}} - u^n_{j-\frac{1}{2},k+\frac{1}{2}}}{2\Delta x} = \frac{1}{2\Delta x}\left(\frac{(\rho u)^n_{j+\frac{3}{2},k+\frac{1}{2}}}{\rho^n_{j+\frac{3}{2},k+\frac{1}{2}}} - \frac{(\rho u)^n_{j-\frac{1}{2},k+\frac{1}{2}}}{\rho^n_{j-\frac{1}{2},k+\frac{1}{2}}}\right), \tag{2.17}$$

$$(v_y)^n_{j+\frac{1}{2},k+\frac{1}{2}} := \frac{v^n_{j+\frac{1}{2},k+\frac{3}{2}} - v^n_{j+\frac{1}{2},k-\frac{1}{2}}}{2\Delta y} = \frac{1}{2\Delta y}\left(\frac{(\rho v)^n_{j+\frac{1}{2},k+\frac{3}{2}}}{\rho^n_{j+\frac{1}{2},k+\frac{3}{2}}} - \frac{(\rho v)^n_{j+\frac{1}{2},k-\frac{1}{2}}}{\rho^n_{j+\frac{1}{2},k-\frac{1}{2}}}\right). \tag{2.18}$$

III. SCHEME ADAPTION ALGORITHM

In this section, we use the pressure-based AIs designed in Section 2 to build simple scheme adaption algorithms in both the 1-D and 2-D cases.

A. One-Dimensional Scheme Adaption Algorithm

We implement the proposed scheme adaption strategy in the framework of semidiscrete finite-volume methods, in which the cell averages $\overline{\boldsymbol{q}}_j(t)$ are evolved in time according to the following system of ODEs:

$$\frac{d}{dt}\overline{\boldsymbol{q}}_j(t) = -\frac{\boldsymbol{H}_{j+\frac{1}{2}}(t) - \boldsymbol{H}_{j-\frac{1}{2}}(t)}{\Delta x}.$$

Here, $\boldsymbol{H}_{j+\frac{1}{2}}$ are numerical fluxes that typically depend on the left- and right-sided values of $\boldsymbol{q}$ at the interface:

$$\boldsymbol{H}_{j+\frac{1}{2}}(t) = \boldsymbol{H}(\boldsymbol{q}^-_{j+\frac{1}{2}}(t), \boldsymbol{q}^+_{j+\frac{1}{2}}(t)), \tag{3.1}$$

where $\boldsymbol{q}^\pm_{j+\frac{1}{2}}(t) := \tilde{\boldsymbol{q}}\left(x_{j+\frac{1}{2}} \pm 0, t\right)$. From here on we suppress the time-dependence of all indexed quantities in order to shorten the notation.

The key idea of our scheme adaption algorithm is the way the point values of $\boldsymbol{q}$ at the cell interfaces are computed. In the smooth parts of the computed solution, we use the nonlimited fifth-order reconstruction, that is, in a "smooth" cell j we take a polynomial piece

$$\mathcal{P}_j(x) = \boldsymbol{q}_j + (\boldsymbol{q}_x)_j(x - x_j) + \frac{1}{2}(\boldsymbol{q}_{xx})_j(x - x_j)^2 + \frac{1}{6}(\boldsymbol{q}_{xxx})_j(x - x_j)^3 + \frac{1}{24}(\boldsymbol{q}_{xxxx})_j(x - x_j)^4$$

that satisfies the following five conservation properties:

$$\frac{1}{\Delta x}\int_{I_{j+m}} \mathcal{P}_j(x)dx = \overline{\boldsymbol{q}}_{j+m}, \quad m \in \{-2, -1, 0, 1, 2\}.$$

The values of this reconstruction at the left and right edges of cell j are

$$\begin{aligned} \boldsymbol{q}^+_{j-\frac{1}{2}} &= \frac{1}{60}\left(2\overline{\boldsymbol{q}}_{j-2} - 13\overline{\boldsymbol{q}}_{j-1} + 47\overline{\boldsymbol{q}}_j + 27\overline{\boldsymbol{q}}_{j+1} - 3\overline{\boldsymbol{q}}_{j+2}\right), \\ \boldsymbol{q}^-_{j+\frac{1}{2}} &= \frac{1}{60}\left(-3\overline{\boldsymbol{q}}_{j-2} + 27\overline{\boldsymbol{q}}_{j-1} + 47\overline{\boldsymbol{q}}_j - 13\overline{\boldsymbol{q}}_{j+1} + 2\overline{\boldsymbol{q}}_{j+2}\right), \end{aligned} \tag{3.2}$$

respectively.

In the "rough" parts of the computed solution we switch to the limited second-order reconstruction (1.4) with the slopes $(\boldsymbol{q}_x)_j$ computed using the generalized minmod limiter [3–6]:

$$(\boldsymbol{q}_x)_j = \text{minmod}\left(\theta\frac{\overline{\boldsymbol{q}}_j - \overline{\boldsymbol{q}}_{j-1}}{\Delta x}, \frac{\overline{\boldsymbol{q}}_{j+1} - \overline{\boldsymbol{q}}_{j-1}}{2\Delta x}, \theta\frac{\overline{\boldsymbol{q}}_{j+1} - \overline{\boldsymbol{q}}_j}{\Delta x}\right), \quad \theta \in [1,2], \tag{3.3}$$

where the minmod function,

$$\text{minmod}(z_1, z_2, ...) := \begin{cases} \min\limits_j\{z_j\}, & \text{if } z_j > 0\ \forall j, \\ \max\limits_j\{z_j\}, & \text{if } z_j < 0\ \forall j, \\ 0, & \text{otherwise,} \end{cases} \tag{3.4}$$

is applied to the vector quantities in (3.3) in a component-wise manner. We can then obtain the limited point values at the edges of the cell j by

$$\boldsymbol{q}^+_{j-\frac{1}{2}} = \overline{\boldsymbol{q}}_j - \frac{\Delta x}{2}(\boldsymbol{q}_x)_j, \quad \boldsymbol{q}^-_{j+\frac{1}{2}} = \overline{\boldsymbol{q}}_j + \frac{\Delta x}{2}(\boldsymbol{q}_x)_j. \tag{3.5}$$

Then, one must decide which reconstruction to use at a given cell. The decision will be made based on the value of the AI at the nearby cell interfaces according to the following algorithm.

Algorithm 3.1 (1-D Scheme Adaption)**.**

1. Compute $\boldsymbol{q}_{j+\frac{1}{2}} := \boldsymbol{q}^-_{j+\frac{1}{2}}$ throughout the entire computational domain using (3.1).
2. Use these values together with the corresponding nonlimited point values stored from the previous time level to evaluate $E^{n-\frac{1}{2}}_{j+\frac{1}{2}}$ by (2.9).
3. Calculate the L^1-norm of the WLR:

$$||E^{n-\frac{1}{2}}||_1 := \sum_j |E^{n-\frac{1}{2}}_{j+\frac{1}{2}}|\Delta x. \tag{3.6}$$

4. Choose an adaption constant $K > 0$.
5. For each j_0 such that $|j_0 + \frac{1}{2} - j| \le \frac{3}{2}$ and

$$|E^{n-\frac{1}{2}}_{j+\frac{1}{2}}| \ge K||E^{n-\frac{1}{2}}||_1, \tag{3.7}$$

compute $\boldsymbol{q}^+_{j_0-\frac{1}{2}}$ and $\boldsymbol{q}^-_{j_0+\frac{1}{2}}$ using the minmod limiter by (3.5). Otherwise, use the nonlimited values (3.1) in cell j instead.

Remark 3.1. In Step 1 one can compute the right-sided values, $\boldsymbol{q}^+_{j+\frac{1}{2}}$, instead of the left-sided ones. These values (or any convex combination of $\boldsymbol{q}^-_{j+\frac{1}{2}}$ and $\boldsymbol{q}^+_{j+\frac{1}{2}}$) can be then used as the point values of $\boldsymbol{q}_{j+\frac{1}{2}}$ in the computation of $E^{n-\frac{1}{2}}_{j+\frac{1}{2}}$ in Step 2.

Remark 3.2. Since the nonlimited fifth-order reconstruction is very oscillatory near jump discontinuities, we prefer to use the nonlimited point values in Step 2. This helps the AI to better detect "rough" parts of the solution than if the limited values were used.

Remark 3.3. Step 5 can be reformulated as follows: We go through each cell interface and if (3.7) holds at interface $j+\frac{1}{2}$, we mark the four nearby cells, $\{j-1, j, j+1, j+2\}$, as belonging to the "rough" part of the solution. We then use the second-order limited reconstruction in the marked cells only, while the nonlimited fifth-order piecewise polynomial reconstruction is utilized elsewhere.

Remark 3.4. As one can see in Figs. 1, 4, and 5 below, the AI typically exhibits very oscillatory behavior. Therefore, one may prefer to use a smoothed version of the AI obtained, for example, by replacing $E^{n-\frac{1}{2}}_{j+\frac{1}{2}}$ with

$$\varepsilon^{n-\frac{1}{2}}_{j+\frac{1}{2}} = \frac{1}{4}\left(|E^{n-\frac{1}{2}}_{j-\frac{1}{2}}| + 2|E^{n-\frac{1}{2}}_{j+\frac{1}{2}}| + |E^{n-\frac{1}{2}}_{j+\frac{3}{2}}|\right)$$

in Steps 2, 3, and 5.

Remark 3.5. Notice that like in many other adaption approaches, we have an adaption constant K, which has to be tuned. We follow the idea in [27, 36] and after tuning K on a coarse grid, we use the same K for finer meshes. In all of the conducted numerical experiments, including the ones reported in Section 4, this strategy proved to be reliable.

B. Two-Dimensional Scheme Adaption Algorithm

In this section, we extend the scheme adaption algorithm presented in Section III A to the 2-D case. As in 1-D, the cell averages

$$\overline{\boldsymbol{q}}_{j,k}(t) :\approx \iint_{I_{j,k}} \boldsymbol{q}(x,y;t)dxdy, \quad I_{j,k} := (x_{j-\frac{1}{2}}, x_{j+\frac{1}{2}}) \times (y_{k-\frac{1}{2}}, y_{k+\frac{1}{2}}),$$

are evolved in time according to the system of ODEs

$$\frac{d}{dt}\overline{\boldsymbol{q}}_{j,k}(t) = -\frac{\boldsymbol{H}^x_{j+\frac{1}{2},k}(t) - \boldsymbol{H}^x_{j-\frac{1}{2},k}(t)}{\Delta x} - \frac{\boldsymbol{H}^y_{j,k+\frac{1}{2}}(t) - \boldsymbol{H}^y_{j,k-\frac{1}{2}}(t)}{\Delta y}, \tag{3.8}$$

where $\boldsymbol{H}^x_{j+\frac{1}{2},k}$ and $\boldsymbol{H}^y_{j,k+\frac{1}{2}}$ are numerical fluxes that typically depend on the edge values of $\boldsymbol{q}$ at the cell interfaces:

$$\begin{aligned} \boldsymbol{H}^x_{j+\frac{1}{2},k}(t) &:= \boldsymbol{H}^x(\tilde{\boldsymbol{q}}(x_{j+\frac{1}{2}}+0,y;t), \tilde{\boldsymbol{q}}(x_{j+\frac{1}{2}}-0,y;t)), \quad y \in (y_{k-\frac{1}{2}}, y_{k+\frac{1}{2}}),\\ \boldsymbol{H}^y_{j,k+\frac{1}{2}}(t) &:= \boldsymbol{H}^y(\tilde{\boldsymbol{q}}(x,y_{k+\frac{1}{2}}+0;t), \tilde{\boldsymbol{q}}(x,y_{k+\frac{1}{2}}-0;t)), \quad x \in (x_{j-\frac{1}{2}}, x_{j+\frac{1}{2}}). \end{aligned} \tag{3.9}$$

Here, $\tilde{\boldsymbol{q}}(x,y;t)$ is a piecewise polynomial approximation,

$$\tilde{\boldsymbol{q}}(x,y;t) = \sum_{j,k} \chi_{I_{j,k}} \mathcal{P}_{j,k}(x,y;t),$$

reconstructed from the available cell averages of $\boldsymbol{q}$. Again, from here on we suppress the time-dependence of all indexed quantities to simplify the notation. Note that each particular numerical flux, (3.9), depends only on several discrete values of $\tilde{\boldsymbol{q}}(x_{j+\frac{1}{2}} \pm 0, y)$ or $\tilde{\boldsymbol{q}}(x, y_{k+\frac{1}{2}} \pm 0)$. For example, in our experiments we have used the numerical fluxes, which are based on the reconstructed

values of $\boldsymbol{q}$ at the centers of the sides and at corners of the cells, that is, every numerical flux depends on 6 reconstructed point values only:

$$\begin{aligned}\boldsymbol{H}^x_{j+\frac{1}{2},k} &= \boldsymbol{H}^x(\tilde{\boldsymbol{q}}(x_{j+\frac{1}{2}}\pm 0, y_{k-\frac{1}{2}}+0), \tilde{\boldsymbol{q}}(x_{j+\frac{1}{2}}\pm 0, y_k), \tilde{\boldsymbol{q}}(x_{j+\frac{1}{2}}\pm 0, y_{k+\frac{1}{2}}-0)),\\ \boldsymbol{H}^y_{j,k+\frac{1}{2}} &= \boldsymbol{H}^y(\tilde{\boldsymbol{q}}(x_{j-\frac{1}{2}}+0, y_{k+\frac{1}{2}}\pm 0), \tilde{\boldsymbol{q}}(x_j, y_{k+\frac{1}{2}}\pm 0), \tilde{\boldsymbol{q}}(x_{j+\frac{1}{2}}-0, y_{k+\frac{1}{2}}\pm 0)).\end{aligned} \tag{3.10}$$

The key idea of our scheme adaption algorithm is the way the point values of $\boldsymbol{q}$ along the cell interfaces are reconstructed. In the smooth parts of the computed solution, we use a nonlimited high-order reconstruction, that is, in a "smooth" cell j, k we take a polynomial piece

$$\begin{aligned}\mathcal{P}_{j,k}(x,y) = {}& \boldsymbol{q}_{j,k} + (\boldsymbol{q}_x)_{j,k}(x-x_j) + (\boldsymbol{q}_y)_{j,k}(y-y_k)\\ &+\frac{1}{2}\left[(\boldsymbol{q}_{xx})_{j,k}(x-x_j)^2 + (\boldsymbol{q}_{yy})_{j,k}(y-y_k)^2\right] + (\boldsymbol{q}_{xy})_{j,k}(x-x_j)(y-y_k)\\ &+\frac{1}{6}\left[(\boldsymbol{q}_{xxx})_{j,k}(x-x_j)^3 + (\boldsymbol{q}_{yyy})_{j,k}(y-y_k)^3\right]\\ &+\frac{1}{2}\left[(\boldsymbol{q}_{xxy})_{j,k}(x-x_j)^2(y-y_k) + (\boldsymbol{q}_{xyy})_{j,k}(x-x_j)(y-y_k)^2\right]\\ &+\frac{1}{24}\left[(\boldsymbol{q}_{xxxx})_{j,k}(x-x_j)^4 + (\boldsymbol{q}_{yyyy})_{j,k}(y-y_k)^4\right] + \frac{1}{4}(\boldsymbol{q}_{xxyy})_{j,k}(x-x_j)^2(y-y_k)^2\end{aligned} \tag{3.11}$$

that satisfies the following 13 conservation properties:

$$\frac{1}{\Delta x\Delta y}\int_{I_{j+m,k+\ell}} \mathcal{P}_{j,k}(x,y)dxdy = \overline{\boldsymbol{q}}_{j+m,k+\ell}, \quad \{m,\ell\in\mathbb{Z} : |m|+|\ell|\le 2\}.$$

One can show that this reconstruction is fourth-order accurate. The values of this reconstruction at the center of four sides, as well as at the corner points of cell (j, k), can be expressed as a linear combination of $\overline{\boldsymbol{q}}_{j,k}$ and the neighboring cell averages. Their explicit forms can be found in [36, Appendix B]. To evaluate the AI, we will use the point value in the northeast corner of each cell, namely,

$$\begin{aligned}\boldsymbol{q}^{\mathrm{NE}}_{j,k} &:= \tilde{\boldsymbol{q}}(x_{j+\frac{1}{2}}-0, y_{k+\frac{1}{2}}-0)\\ &= \frac{1}{180}[107\overline{\boldsymbol{q}}_{j,k} + 20\overline{\boldsymbol{q}}_{j+1,k+1} + 5\overline{\boldsymbol{q}}_{j-1,k-1} - 10(\overline{\boldsymbol{q}}_{j-1,k+1} + \overline{\boldsymbol{q}}_{j+1,k-1}) + 71(\overline{\boldsymbol{q}}_{j,k+1} + \overline{\boldsymbol{q}}_{j+1,k})\\ &\quad -34(\overline{\boldsymbol{q}}_{j,k-1} + \overline{\boldsymbol{q}}_{j-1,k}) + 6(\overline{\boldsymbol{q}}_{j-2,k} + \overline{\boldsymbol{q}}_{j,k-2}) - 9(\overline{\boldsymbol{q}}_{j,k+2} + \overline{\boldsymbol{q}}_{j+2,k})].\end{aligned} \tag{3.12}$$

In the "rough" parts of the computed solution, we switch to a limited second-order reconstruction,

$$\tilde{\boldsymbol{q}}(x,y) = \overline{\boldsymbol{q}}_{j,k} + (\boldsymbol{q}_x)_{j,k}(x-x_j) + (\boldsymbol{q}_y)_{j,k}(y-y_j), \quad (x,y)\in I_{j,k}, \tag{3.13}$$

where, as in the 1-D case, the slopes are computed using the generalized minmod limiter:

$$\begin{aligned}(\boldsymbol{q}_x)_{j,k} &= \mathrm{minmod}\Big(\theta\frac{\overline{\boldsymbol{q}}_{j,k}-\overline{\boldsymbol{q}}_{j-1,k}}{\Delta x}, \frac{\overline{\boldsymbol{q}}_{j+1,k}-\overline{\boldsymbol{q}}_{j-1,k}}{2\Delta x}, \theta\frac{\overline{\boldsymbol{q}}_{j+1,k}-\overline{\boldsymbol{q}}_{j,k}}{\Delta x}\Big),\\ (\boldsymbol{q}_y)_{j,k} &= \mathrm{minmod}\Big(\theta\frac{\overline{\boldsymbol{q}}_{j,k}-\overline{\boldsymbol{q}}_{j,k-1}}{\Delta y}, \frac{\overline{\boldsymbol{q}}_{j,k+1}-\overline{\boldsymbol{q}}_{j,k-1}}{2\Delta y}, \theta\frac{\overline{\boldsymbol{q}}_{j,k+1}-\overline{\boldsymbol{q}}_{j,k}}{\Delta y}\Big), \quad \theta\in[1,2].\end{aligned}$$

One must now decide which 2-D reconstruction to use in each cell. The decision will be made based on the value of the pressure-based AI, (2.16), at the nearby cell corners according to the following algorithm.

Algorithm 3.2 (2-D Scheme Adaption)**.**

1. Compute $\boldsymbol{q}_{j+\frac{1}{2},k+\frac{1}{2}} := \boldsymbol{q}^{\mathrm{NE}}_{j,k}$ throughout the entire computational domain using (3.12).
2. Use these values together with the corresponding nonlimited point values stored from the previous time level to evaluate $E^{n-\frac{1}{2}}_{j+\frac{1}{2},k+\frac{1}{2}}$ by (2.16).
3. Calculate the L^1-norm of the WLR:

$$||E^{n-\frac{1}{2}}||_1 := \sum_{j,k} |E^{n-\frac{1}{2}}_{j+\frac{1}{2},k+\frac{1}{2}}|\Delta x \Delta y.$$

4. Choose an adaption constant $K > 0$.
5. For each (j_0, k_0) such that both $|j_0 + \frac{1}{2} - j| \le \frac{3}{2}$ and $|k_0 + \frac{1}{2} - k| \le \frac{3}{2}$, and

$$|E^{n-\frac{1}{2}}_{j+\frac{1}{2},k+\frac{1}{2}}| \ge K||E^{n-\frac{1}{2}}||_1, \tag{3.14}$$

use the second-order limited reconstruction (3.13) in cell (j_0, k_0). Otherwise use the nonlimited high-order reconstruction (3.11) there.

Remark 3.6. In Step 1, one can compute alternative point values at $(x_{j+\frac{1}{2}}, y_{k+\frac{1}{2}})$. This means that in the computation of $E^{n-\frac{1}{2}}_{j+\frac{1}{2},k+\frac{1}{2}}$ in Step 2, any of the following four point values, $\tilde{\boldsymbol{q}}(x_{j+\frac{1}{2}} \pm 0, y_{k+\frac{1}{2}} \pm 0)$, or any of their convex combinations can be used (see Remark 4.2 in Example 5).

Remark 3.7. Since the nonlimited high-order reconstruction is very oscillatory near jump discontinuities, we prefer to use the nonlimited point values in Step 2. This helps the AI to better detect "rough" parts of the solution than if the limited values were used.

Remark 3.8. Step 5 can be reformulated as follows: We go through each cell corner and if (3.14) holds at $(x_{j+\frac{1}{2}}, y_{k+\frac{1}{2}})$, we mark the 16 nearby cells (j_0, k_0) such that $j_0 \in \{j-1, j, j+1, j+2\}$ and $k_0 \in \{k-1, k, k+1, k+2\}$, as belonging to the "rough" part of the computed solution. We then use the second-order limited reconstruction in the marked cells only, while the nonlimited fourth-order piecewise polynomial reconstruction is utilized elsewhere.

Remark 3.9. The AI typically exhibits very oscillatory behavior, therefore one may prefer to use a smoothed version of the AI obtained, for example, by replacing $E^{n-\frac{1}{2}}_{j+\frac{1}{2},k+\frac{1}{2}}$ with

$$\varepsilon^{n-\frac{1}{2}}_{j+\frac{1}{2},k+\frac{1}{2}} = \frac{1}{16}\Big(|E^{n-\frac{1}{2}}_{j-\frac{1}{2},k-\frac{1}{2}}| + 2|E^{n-\frac{1}{2}}_{j-\frac{1}{2},k+\frac{1}{2}}| + |E^{n-\frac{1}{2}}_{j-\frac{1}{2},k+\frac{3}{2}}|$$
$$2|E^{n-\frac{1}{2}}_{j+\frac{1}{2},k-\frac{1}{2}}| + 4|E^{n-\frac{1}{2}}_{j+\frac{1}{2},k+\frac{1}{2}}| + 2|E^{n-\frac{1}{2}}_{j+\frac{1}{2},k+\frac{3}{2}}|$$

$$|E^{n-\frac{1}{2}}_{j+\frac{3}{2},k-\frac{1}{2}}| + 2|E^{n-\frac{1}{2}}_{j+\frac{3}{2},k+\frac{1}{2}}| + |E^{n-\frac{1}{2}}_{j+\frac{3}{2},k+\frac{3}{2}}|\Big)$$

in Steps 2, 3, and 5.

Remark 3.10. As in the 1-D algorithm, we have an adaption constant K, which has to be tuned. Once again, we follow the idea in [27, 36] and after tuning K on a coarse grid, we use the same value of K in finer mesh computations.

Remark 3.11. We would like to emphasize that the proposed scheme adaption strategy is probably the simplest one. In principle, the sharp switch in step 5 in both Algorithm 3.1 and 3.2 can be replaced with a smooth one by taking a proper convex combination of nonlimited higher-order and limited second-order point values at the cell interfaces. This can be done in a way similar to the approach used in WENO schemes, see, e.g., [9] and references therein. However, in this paper our main goal is to demonstrate the capability of the proposed pressure-based AI to automatically distinguish between shock and contact waves and this goal can be achieved using the simple scheme adaption Algorithms 3.1 and 3.2.

IV. NUMERICAL EXPERIMENTS

In this section, we demonstrate the experimental rates of decay of the designed pressure-based AIs in both a 1-D and 2-D examples. We also demonstrate the performance of the proposed scheme adaption algorithm on a number of 1-D and 2-D examples. In all of the examples below, $\gamma = 1.4$ (except for Example 2, where we take $\gamma = 5/3$) and the CFL number is 0.5. The time evolution is always performed using the third-order SSP Runge-Kutta method, see [37, 38].

Remark 4.1. As the AI uses the data from two consecutive time levels, the first step in time must be made using a second-order limited reconstruction applied throughout the entire computational domain.

A. One-Dimensional Central-Upwind Numerical Flux

To implement the 1-D scheme adaption algorithm described in Section 3.1, we need to specify the numerical flux to be used in (3.1). Our particular choice is the central-upwind flux derived in [32]:

$$\boldsymbol{H}_{j+\frac{1}{2}} = \frac{a^+_{j+\frac{1}{2}}\boldsymbol{f}(\boldsymbol{q}^-_{j+\frac{1}{2}}) - a^-_{j+\frac{1}{2}}\boldsymbol{f}(\boldsymbol{q}^+_{j+\frac{1}{2}})}{a^+_{j+\frac{1}{2}} - a^-_{j+\frac{1}{2}}} + \frac{a^+_{j+\frac{1}{2}}a^-_{j+\frac{1}{2}}\left[(\boldsymbol{q}^+_{j+\frac{1}{2}} - \boldsymbol{q}^-_{j+\frac{1}{2}}) - \boldsymbol{d}_{j+\frac{1}{2}}\right]}{a^+_{j+\frac{1}{2}} - a^-_{j+\frac{1}{2}}},$$

where the one-sided local speeds $a^{\pm}_{j+\frac{1}{2}}$ are estimated using the largest and smallest eigenvalues of the Jacobian $\frac{\partial \boldsymbol{f}}{\partial \boldsymbol{q}}$ as follows:

$$a^+_{j+\frac{1}{2}} = \max\left\{u^+_{j+\frac{1}{2}} + \sqrt{\frac{\gamma p^+_{j+\frac{1}{2}}}{\rho^+_{j+\frac{1}{2}}}}, u^-_{j+\frac{1}{2}} + \sqrt{\frac{\gamma p^-_{j+\frac{1}{2}}}{\rho^-_{j+\frac{1}{2}}}}, 0\right\},$$

$$a^-_{j+\frac12} = \min\left\{u^+_{j+\frac12} - \sqrt{\frac{\gamma p^+_{j+\frac12}}{\rho^+_{j+\frac12}}}, u^-_{j+\frac12} - \sqrt{\frac{\gamma p^-_{j+\frac12}}{\rho^-_{j+\frac12}}}, 0\right\}.$$

The term $\boldsymbol{d}_{j+\frac12}$ is a "built-in" antidiffusion (see [32] for details):

$$\boldsymbol{d}_{j+\frac12} = \alpha \cdot \text{minmod}\left(\boldsymbol{q}^+_{j+\frac12} - \boldsymbol{q}^*_{j+\frac12}, \boldsymbol{q}^*_{j+\frac12} - \boldsymbol{q}^-_{j+\frac12}\right),$$

where

$$\boldsymbol{q}^*_{j+\frac12} = \frac{a^+_{j+\frac12}\boldsymbol{q}^+_{j+\frac12} - a^-_{j+\frac12}\boldsymbol{q}^-_{j+\frac12} - (\boldsymbol{f}(\boldsymbol{q}^+_{j+\frac12}) - \boldsymbol{f}(\boldsymbol{q}^-_{j+\frac12}))}{a^+_{j+\frac12} - a^-_{j+\frac12}}$$

and $\alpha \in [0,1]$ is a parameter that can be used to regulate the amount of antidiffusion in the central-upwind flux.

B. Rates of Decay of the One-Dimensional Pressure-Based AI

In this section, we examine the rates of decay of our new 1-D pressure-based AI. To this end, we consider the 1-D system, (1.1), (1.2), subject to the Sod initial data:

$$(\rho, u, p)(x,0) = \begin{cases}(1.000, 0, 1.0), & x < 0.5,\\ (0.125, 0, 0.1), & x > 0.5.\end{cases} \tag{4.1}$$

We first compute the numerical solution of the initial value problem (1.1), (1.2), (4.1), at the final time $t^N = 0.16$ using the second-order central-upwind scheme with the minmod parameter $\theta = 1.3$, "built-in" antidiffusion parameter $\alpha = 0$ and fixed $\Delta t = 0.2\Delta x$. We then use (2.9), (2.10) to calculate the values of $||E^{N-\frac12}||_{L^\infty_{\text{loc}}}$ in different parts of the computational domain. The obtained results are presented in Fig. 1 and Table I.

As can be seen in Table I, the local decay rates around the rarefaction corner and contact wave are somewhat erratic, however, the magnitude of the WLR is much smaller there than around the shock wave (notice that since the value of the WLR is largest in the shock area, the global maximum of the WLR coincides with its local maximum at the shock). This suggests that the pressure-based AI can be used to identify shock regions and to automatically distinguish them from other nonsmooth parts of the computed solution.

C. One-Dimensional Numerical Experiments

In this section, we compare a second-order minmod limited scheme to our proposed scheme adaption method. The minmod parameter $\theta = 1.3$ and the "antidiffusion" coefficient $\alpha = 1$ are used in all of the 1-D experiments except for Example 2, where we take $\alpha = 0$. The adaption constant K is chosen per experiment.

Example 1 (Moving Contact Wave)**.** In the first example, we consider a single moving contact wave corresponding to the following initial data:

$$(\rho, u, p)(x,0) = \begin{cases}(1.4, 0.1, 1), & x < 0.5,\\ (1, 0.1, 1), & \text{otherwise.}\end{cases}$$

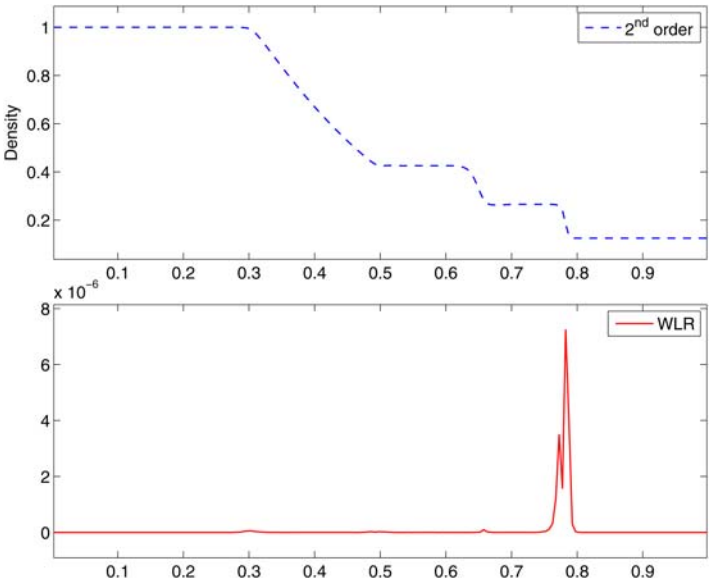

FIG. 1. Solution of the Sod problem computed by the second-order central-upwind scheme on a uniform grid with $\Delta x = 1/200$. The density and magnitude of the WLR are shown on the upper and lower axes, respectively. [Color figure can be viewed in the online issue, which is available at wileyonlinelibrary.com.]

TABLE I. Sod problem: The magnitude of the WLR computed at the final time $t^N = 0.16$.

Δx	$\max_{a\le x_{j+\frac{1}{2}}\le b} \lvert E^{N-\frac{1}{2}}_{j+\frac{1}{2}} \rvert$	Decay rate	Δx	$\max_{a\le x_{j+\frac{1}{2}}\le b} \lvert E^{N-\frac{1}{2}}_{j+\frac{1}{2}} \rvert$	Decay rate
Rarefaction corner, $a = 0.25$, $b = 0.35$			Contact wave, $a = 0.6$, $b = 0.7$		
1/100	5.007 e − 06	–	1/100	5.571 e − 07	–
1/200	5.201 e − 07	3.27	1/200	3.342 e − 07	0.74
1/400	3.294 e − 07	0.66	1/400	7.160 e − 08	2.22
1/800	1.136 e − 07	1.54	1/800	4.730 e − 08	0.60
1/1600	8.821 e − 09	3.69	1/1600	2.064 e − 08	1.20
1/3200	4.438 e − 09	0.99	1/3200	7.613 e − 09	1.44
1/6400	1.105 e − 09	2.01	1/6400	4.231 e − 09	0.85
Smooth subregion, $a = 0.35$, $b = 0.45$			Everywhere (Shock), $a = 0$, $b = 1$		
1/100	1.299 e − 07	–	1/100	6.349 e − 05	–
1/200	1.062 e − 08	3.61	1/200	3.420 e − 05	0.89
1/400	8.188 e − 10	3.70	1/400	1.895 e − 05	0.85
1/800	6.043 e − 11	3.76	1/800	1.022 e − 05	0.89
1/1600	4.294 e − 12	3.81	1/1600	3.984 e − 06	1.36
1/3200	2.951 e − 13	3.86	1/3200	2.274 e − 06	0.81
1/6400	1.945 e − 14	3.92	1/6400	1.229 e − 06	0.89

In principle, our adaption strategy is designed using the idea that nonlinear limiters are only needed to stabilize nonlinear shock waves, while isolated linear contact waves can be accurately captured using nonlimited high-order schemes. To demonstrate the plausibility of the proposed approach, we use a single contact wave setting. We compute the solution at time $t = 0.2$ using both the fifth-order nonlimited and second-order limited schemes on two uniform grids with $\Delta x = 1/100$

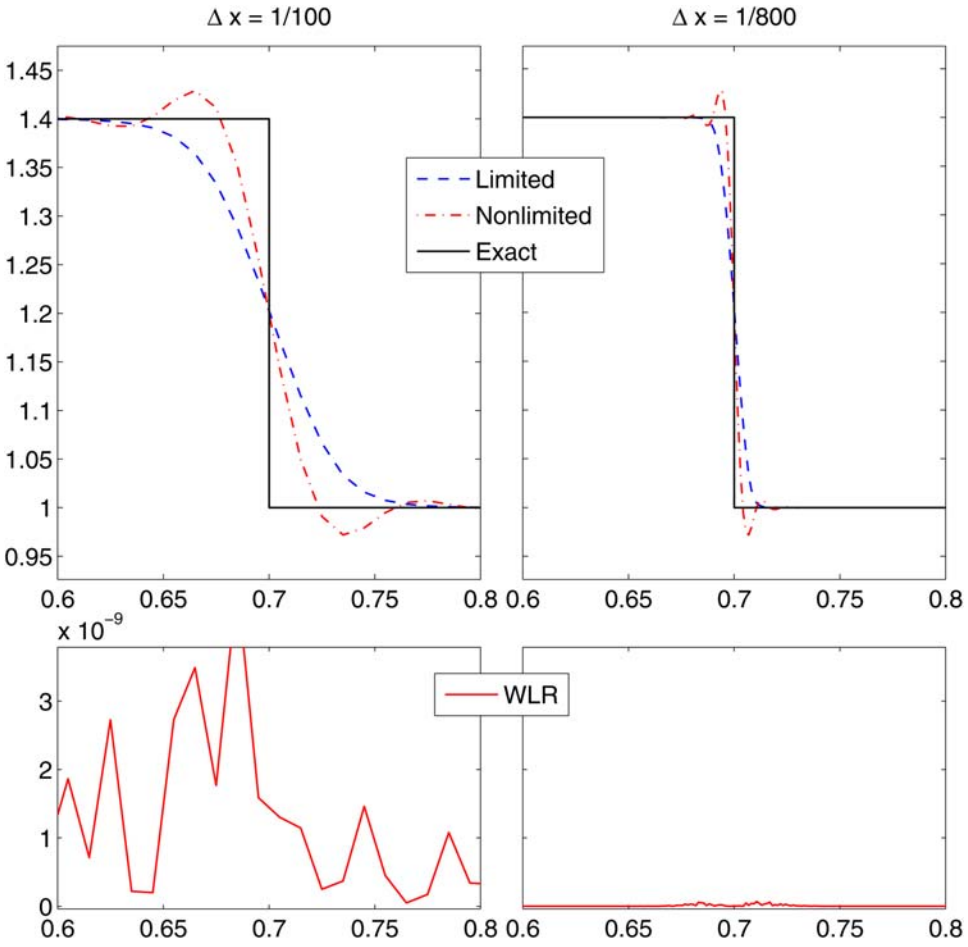

FIG. 2. Example 1: Density profiles computed by the fifth-order nonlimited and second-order limited schemes using coarse ($\Delta x = 1/100$, left) and fine ($\Delta x = 1/800$, right) uniform grids (top row). Corresponding outputs of the magnitude of the WLR computed using the second-order limited scheme are shown in the bottom row. [Color figure can be viewed in the online issue, which is available at wileyonlinelibrary.com.]

and $\Delta x = 1/800$. The obtained results (density) are shown in the upper part of Fig. 2. As one can see, the fifth-order solution is sharper though more oscillatory. The magnitude of oscillations is however relatively small and does not increase when the mesh is refined. The corresponding values of the magnitude of the WLR computed using the second-order limited scheme are shown in the lower part of Fig. 2. The experimental convergence rates for the two schemes are shown in Table II.

Example 2 (Le Blanc Shock-Tube Problem)**.** In this example, we consider a shock-tube problem with the Le Blanc initial data (see, e.g., [39]):

$$(\rho, u, p)(x, 0) = \begin{cases} (1, 0, \frac{2}{3} \cdot 10^{-1}), & x < 3, \\ (10^{-3}, 0, \frac{2}{3} \cdot 10^{-10}), & \text{otherwise.} \end{cases}$$

TABLE II. Example 1: L^1-errors and experimental convergence rates for the fifth-order nonlimited and second-order limited schemes.

Δx	(Nonlimited) $\|\|\rho^\Delta - \rho\|\|_1$	Rate	(Limited) $\|\|\rho^\Delta - \rho\|\|_1$	Rate
1/100	5.476 e − 3	–	8.354 e − 3	–
1/200	3.102 e − 3	0.82	4.889 e − 3	0.77
1/400	1.791 e − 3	0.79	2.854 e − 3	0.78
1/800	1.005 e − 3	0.83	1.668 e − 3	0.77
1/1600	5.701 e − 4	0.82	9.789 e − 4	0.77

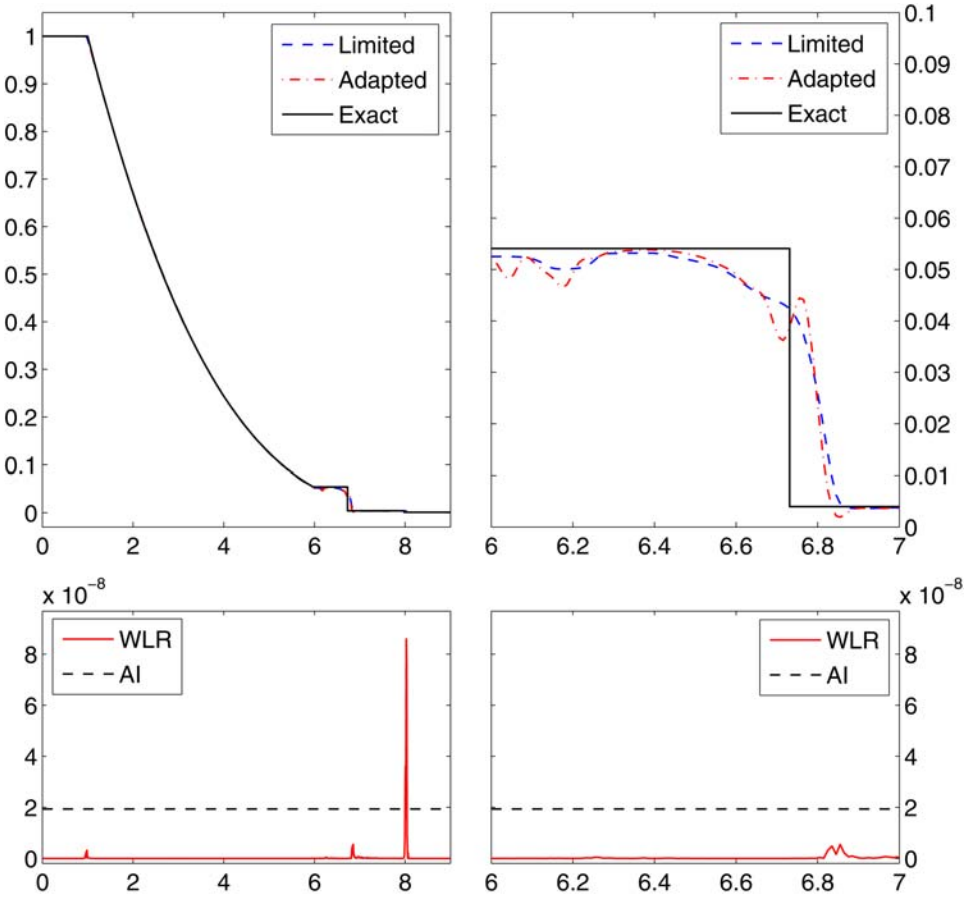

FIG. 3. Example 2: Density profiles (top row) computed by the adapted and second-order limited schemes using a uniform grid with $\Delta x = 1/100$ (left column) and a close up of the contact wave (right column). Corresponding outputs of the magnitude of the WLR computed using the adapted scheme are shown in the bottom row. [Color figure can be viewed in the online issue, which is available at wileyonlinelibrary.com.]

In the upper part of Fig. 3, we plot the numerical solutions at time $t = 6$ computed using the proposed scheme adaption method and the limited second-order central-upwind scheme on a uniform grid with $\Delta x = 1/100$ together with the exact solution. The adaption constant is chosen as $K = 5$. While the magnitude of the WLR (Fig. 3, lower left) shows peaks at the rarefaction corner

TABLE III. Example 2: L^1-errors and experimental convergence rates for the scheme adaption method.

Δx	$\|\|\rho^{\Delta} - \rho\|\|_1$	Rate
1/100	9.262 e − 03	–
1/200	4.716 e − 03	0.97
1/400	2.462 e − 03	0.94
1/800	1.226 e − 03	1.00
1/1600	6.323 e − 04	0.96

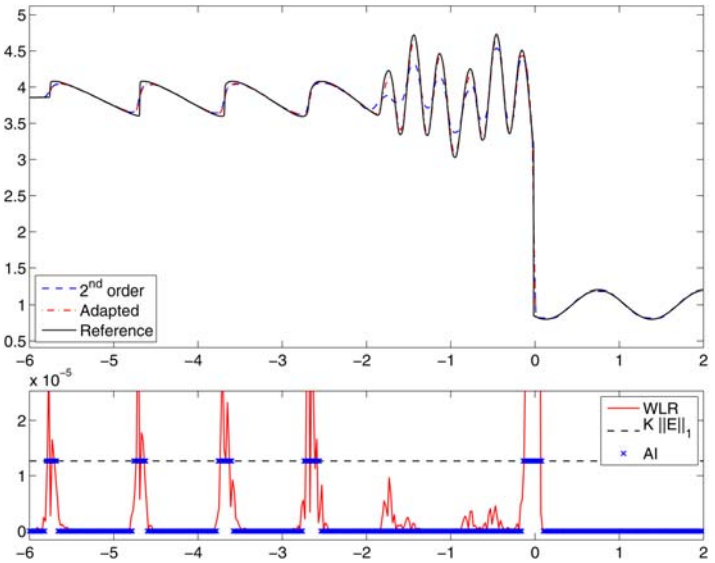

FIG. 4. Example 3: Density profiles computed by the adapted and fully limited schemes together with the reference solution are shown on the upper axis, magnitude of the WLR and the adaption areas are shown on the lower axis. [Color figure can be viewed in the online issue, which is available at wileyonlinelibrary.com.]

and the contact wave, they are much smaller than the peak at the shock. The scheme adaption method provides only a slight improvement in the slope of the contact wave (Fig. 3, upper right). However, even in the case of this extreme shock-tube problem, the oscillations are manageable as shown in the experimental convergence rates in Table III for the scheme adaption method.

Example 3 (Acoustic-Shock Interaction)**.** In this example taken from [30] (see also [40]), we consider an interaction of an acoustic and shock waves. The initial data,

$$(\rho, u, p)(x, 0) = \begin{cases} (3.857143, -0.920279, 10.33333), & x < 0, \\ (1 + \varepsilon \sin(5x), -3.549648, 1), & 0 \le x \le 10, \\ (1, -3.549648, 1), & x > 10, \end{cases}$$

describe a density perturbation moving leftward into a stationary shock of Mach number $M_s = 3$. In this experiment, we take $\varepsilon = 0.2$, $K = 0.3$ and $\Delta x = 1/30$.

In the upper part of Fig. 4, we plot the numerical solutions at time $t = 2$ computed using the proposed scheme adaption method and the limited second-order central-upwind scheme together with the reference solution obtained using the limited scheme with very diffusive parameters,

$\theta = 1$ and $\alpha = 0$, on a fine grid with $\Delta x = 1/1000$. As one can see, the use of high-order piecewise polynomial reconstruction in the oscillatory portion of the solution leads to much higher resolution so that the adaptive solution clearly outperforms the limited second-order one. The obtained solution is in good agreement with the reference solution, even though a relatively coarse grid with $\Delta x = 1/30$ has been used. Also, note that the discontinuities on the left part of the domain are shock waves. As the shock waves emerge from the perturbation, the AI (plotted in the lower part of Fig. 4) is capable of identifying them so that the nonlinear limiter is applied and thus oscillations are avoided.

Example 4 (Woodward-Colella Blast Wave)**.** Next, we consider the Woodward-Colella blast wave problem [41], in which two high-energy fronts interact in a closed domain modeled using the reflecting/solid wall boundary conditions set at $x = 0$ and $x = 1$. The adaption constant K is chosen to be 5 and the solution is computed on the uniform grid with $\Delta x = 1/400$. The initial data are given by

$$(\rho, u, p)(x, 0) = \begin{cases} (1, 0, 1000), & 0 \le x \le 0.1, \\ (1, 0, 0.01), & 0.1 < x < 0.9, \\ (1, 0, 100), & 0.9 \le x \le 1. \end{cases}$$

In Fig. 5, we display solutions (adapted, fully limited and the reference one, obtained by the limited scheme on a fine grid with $\Delta x = 1/4000$) of the blast wave problem at time $t = 0.038$, which is a standard final time in many benchmark tests, and at the later time $t = 0.09$. We also show the corresponding values of AI underneath the density plots. As the two fronts meet, the second-order limited reconstruction lowers the peak near $x \approx 0.77$ as can be seen in the left plot of Fig. 5. The right plot demonstrates that at large times, the adaptive use of the fifth-order reconstruction noticeably reduces the amount of numerical diffusion present in the scheme.

D. Two-Dimensional Central-Upwind Numerical Flux

To implement our 2-D scheme adaption algorithm described in Section 3.2, we need to specify the numerical flux to be used in (3.10). Our particular choice is the central-upwind flux derived in [32]:

$$\begin{aligned} \boldsymbol{H}^x_{j+\frac{1}{2},k}(t) := & \frac{a^+_{j+\frac{1}{2},k}(\boldsymbol{f}(\boldsymbol{q}^{\mathrm{SE}}_{j,k}) + 4\boldsymbol{f}(\boldsymbol{q}^{\mathrm{E}}_{j,k}) + \boldsymbol{f}(\boldsymbol{q}^{\mathrm{NE}}_{j,k}))}{6\left(a^+_{j+\frac{1}{2},k} - a^-_{j+\frac{1}{2},k}\right)} \\ & - \frac{a^-_{j+\frac{1}{2},k}(\boldsymbol{f}(\boldsymbol{q}^{\mathrm{SW}}_{j+1,k}) + 4\boldsymbol{f}(\boldsymbol{q}^{\mathrm{W}}_{j+1,k}) + \boldsymbol{f}(\boldsymbol{q}^{\mathrm{NW}}_{j+1,k}))}{6\left(a^+_{j+\frac{1}{2},k} - a^-_{j+\frac{1}{2},k}\right)} \\ & + a^+_{j+\frac{1}{2},k}a^-_{j+\frac{1}{2},k}\left[\frac{(\boldsymbol{q}^{\mathrm{SE}}_{j,k} + 4\boldsymbol{q}^{\mathrm{E}}_{j,k} + \boldsymbol{q}^{\mathrm{NE}}_{j,k}) - (\boldsymbol{q}^{\mathrm{SW}}_{j+1,k} + 4\boldsymbol{q}^{\mathrm{W}}_{j+1,k} + \boldsymbol{q}^{\mathrm{NW}}_{j+1,k}) - 6\boldsymbol{d}^x_{j+\frac{1}{2},k}}{6\left(a^+_{j+\frac{1}{2},k} - a^-_{j+\frac{1}{2},k}\right)}\right], \end{aligned}$$

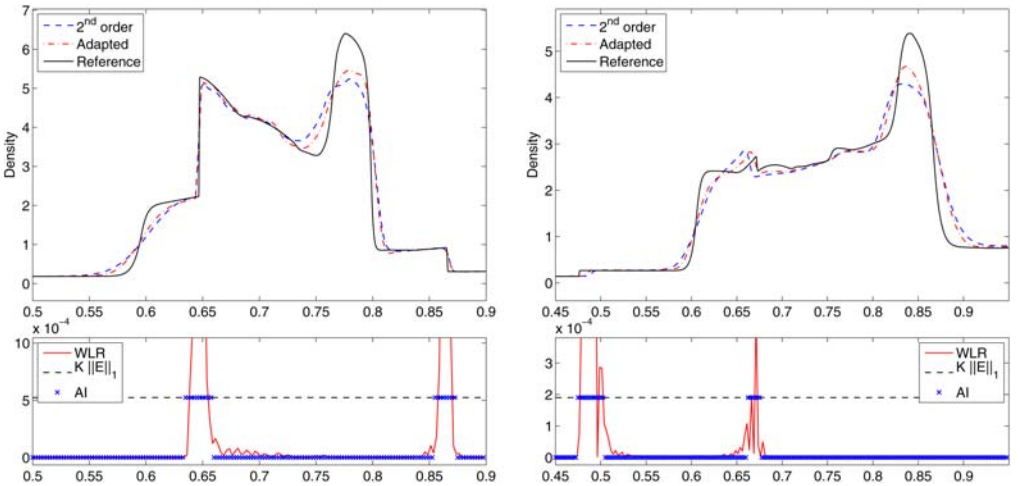

FIG. 5. Example 4: Density profiles computed by the adapted and fully limited schemes together with the reference solution are shown on the upper axis, magnitude of the WLR and the adaption areas shown on the lower axis. The solutions are presented at $t = 0.038$ (left) and $t = 0.09$ (right). [Color figure can be viewed in the online issue, which is available at wileyonlinelibrary.com.]

$$\boldsymbol{H}^{y}_{j,k+\frac{1}{2}}(t) := \frac{b^{+}_{j,k+\frac{1}{2}}\left(\boldsymbol{g}(\boldsymbol{q}^{\mathrm{NW}}_{j,k}) + 4\boldsymbol{g}(\boldsymbol{q}^{\mathrm{N}}_{j,k}) + \boldsymbol{g}(\boldsymbol{q}^{\mathrm{NE}}_{j,k})\right)}{6\left(b^{+}_{j,k+\frac{1}{2}} - b^{-}_{j,k+\frac{1}{2}}\right)}$$
$$- \frac{b^{-}_{j,k+\frac{1}{2}}\left(\boldsymbol{g}(\boldsymbol{q}^{\mathrm{SW}}_{j,k+1}) + 4\boldsymbol{g}(\boldsymbol{q}^{\mathrm{S}}_{j,k+1}) + \boldsymbol{g}(\boldsymbol{q}^{\mathrm{SE}}_{j,k+1})\right)}{6\left(b^{+}_{j,k+\frac{1}{2}} - b^{-}_{j,k+\frac{1}{2}}\right)}$$
$$+ b^{+}_{j,k+\frac{1}{2}} b^{-}_{j,k+\frac{1}{2}} \left[\frac{(\boldsymbol{q}^{\mathrm{NW}}_{j,k} + 4\boldsymbol{q}^{\mathrm{N}}_{j,k} + \boldsymbol{q}^{\mathrm{NE}}_{j,k}) - (\boldsymbol{q}^{\mathrm{SW}}_{j,k+1} + 4\boldsymbol{q}^{\mathrm{S}}_{j,k+1} + \boldsymbol{q}^{\mathrm{SE}}_{j,k+1}) - 6\boldsymbol{d}^{y}_{j,k+\frac{1}{2}}}{6\left(b^{+}_{j,k+\frac{1}{2}} - b^{-}_{j,k+\frac{1}{2}}\right)}\right],$$

where the one-sided local speeds in the x- and y-directions, $a^{\pm}_{j+\frac{1}{2},k}$ and $b^{\pm}_{j,k+\frac{1}{2}}$, are estimated using the largest and smallest eigenvalues of the Jacobians $\frac{\partial f}{\partial \boldsymbol{q}}$ and $\frac{\partial \boldsymbol{g}}{\partial \boldsymbol{q}}$, respectively:

$$a^{+}_{j+\frac{1}{2},k} = \max\left\{u^{\mathrm{W}}_{j+1,k} + \sqrt{\frac{\gamma p^{\mathrm{W}}_{j+1,k}}{\rho^{\mathrm{W}}_{j+1,k}}}, u^{\mathrm{E}}_{j,k} + \sqrt{\frac{\gamma p^{\mathrm{E}}_{j,k}}{\rho^{\mathrm{E}}_{j,k}}}, 0\right\},$$
$$a^{-}_{j+\frac{1}{2},k} = \min\left\{u^{\mathrm{W}}_{j+1,k} - \sqrt{\frac{\gamma p^{\mathrm{W}}_{j+1,k}}{\rho^{\mathrm{W}}_{j+1,k}}}, u^{\mathrm{E}}_{j,k} - \sqrt{\frac{\gamma p^{\mathrm{E}}_{j,k}}{\rho^{\mathrm{E}}_{j,k}}}, 0\right\},$$
$$b^{+}_{j,k+\frac{1}{2}} = \max\left\{v^{\mathrm{S}}_{j,k+1} + \sqrt{\frac{\gamma p^{\mathrm{S}}_{j,k+1}}{\rho^{\mathrm{S}}_{j,k+1}}}, v^{\mathrm{N}}_{j,k} + \sqrt{\frac{\gamma p^{\mathrm{N}}_{j,k}}{\rho^{\mathrm{N}}_{j,k}}}, 0\right\},$$

$$b^-_{j,k+\frac{1}{2}} = \max\left\{v^{\rm S}_{j,k+1} - \sqrt{\frac{\gamma p^{\rm S}_{j,k+1}}{\rho^{\rm S}_{j,k+1}}}, v^{\rm N}_{j,k} - \sqrt{\frac{\gamma p^{\rm N}_{j,k}}{\rho^{\rm N}_{j,k}}}, 0\right\}.$$

As in the 1-D case, the terms $\boldsymbol{d}^x_{j+\frac{1}{2},k}$ and $\boldsymbol{d}^y_{j,k+\frac{1}{2}}$ can be viewed as a "built-in" anti-diffusion acting in the x- and y-directions, respectively. These terms have been derived in [32] and read

$$\boldsymbol{d}^x_{j+\frac{1}{2},k} = \alpha\cdot\text{minmod}\left(\boldsymbol{q}^{\rm NW}_{j+1,k} - \boldsymbol{q}^*_{j+\frac{1}{2},k},\quad \boldsymbol{q}^*_{j+\frac{1}{2},k} - \boldsymbol{q}^{\rm NE}_{j,k},\quad \boldsymbol{q}^{\rm SW}_{j+1,k} - \boldsymbol{q}^*_{j+\frac{1}{2},k},\quad \boldsymbol{q}^*_{j+\frac{1}{2},k} - \boldsymbol{q}^{\rm SE}_{j,k}\right),$$
$$\boldsymbol{d}^y_{j,k+\frac{1}{2}} = \alpha\cdot\text{minmod}\left(\boldsymbol{q}^{\rm SW}_{j,k+1} - \boldsymbol{q}^*_{j,k+\frac{1}{2}},\quad \boldsymbol{q}^*_{j,k+\frac{1}{2}} - \boldsymbol{q}^{\rm NW}_{j,k},\quad \boldsymbol{q}^{\rm SE}_{j,k+1} - \boldsymbol{q}^*_{j,k+\frac{1}{2}},\quad \boldsymbol{q}^*_{j,k+\frac{1}{2}} - \boldsymbol{q}^{\rm NE}_{j,k}\right),$$

where

$$\boldsymbol{q}^*_{j+\frac{1}{2},k} = \frac{a^+_{j+\frac{1}{2},k}\boldsymbol{q}^{\rm W}_{j+1,k} - a^-_{j+\frac{1}{2},k}\boldsymbol{q}^{\rm E}_{j,k} - \left(\boldsymbol{f}(\boldsymbol{q}^{\rm W}_{j+1,k}) - \boldsymbol{f}(\boldsymbol{q}^{\rm E}_{j,k})\right)}{a^+_{j+\frac{1}{2},k} - a^-_{j+\frac{1}{2},k}}$$
$$\boldsymbol{q}^*_{j,k+\frac{1}{2}} = \frac{b^+_{j,k+\frac{1}{2}}\boldsymbol{q}^{\rm S}_{j,k+1} - b^-_{j,k+\frac{1}{2}}\boldsymbol{q}^{\rm N}_{j,k} - \left(\boldsymbol{g}(\boldsymbol{q}^{\rm S}_{j,k+1}) - \boldsymbol{g}(\boldsymbol{q}^{\rm N}_{j,k})\right)}{b^+_{j,k+\frac{1}{2}} - b^-_{j,k+\frac{1}{2}}}$$

and $\alpha \in [0,1]$ is a parameter that can be used to regulate the amount of antidiffusion in the central-upwind flux.

E. Rates of Decay of the Two-Dimensional Pressure-Based AI

In this section, we examine the rates of decay of our new 2-D pressure-based AI. To this end, we consider the system (2.11), (2.12) subject to initial data taken from [42] (see also [32, 43], where different numerical schemes were tested on this problem). The initial data are radially symmetric and we set

$$(\overline{\rho}^0_{j,k}, u^0_{j,k}, v^0_{j,k}, p^0_{j,k}) = \begin{cases}(1,0,0,1), & x_j^2 + y_k^2 < 0.16,\\ (0.1,0,0,0.1), & \text{otherwise.}\end{cases}$$

Due to the symmetry of the problem, the computations are carried out in the domain $[0,1.5]\times[0,1.5]$ using the uniform grid with $\Delta x = \Delta y = 3/800$, reflecting boundary conditions at $x=0$ and $y=0$, and free boundary conditions at $x=1.5$ and $y=1.5$.

We compute the solution until the final time $t^N = 3.2$ using the fully limited second-order central-upwind scheme with the minmod parameter $\theta = 1.3$ and "built-in" antidiffusion parameter $\alpha = 1$. We then use (2.16), (2.18) to calculate the values of $||E^{N-\frac{1}{2}}||_{L^\infty_{\rm loc}}$ in different parts of the computational domain. The obtained results are presented in Table IV.

As can be seen in Table IV, the local decay rates around the rarefaction edge and contact wave are somewhat erratic, however, the magnitude of the WLR is much smaller there than around the shock wave (notice that since the value of the WLR is largest in the shock area, the global maximum of the WLR coincides with its local maximum at the shock). As in the 1-D case, the size of the WLR at the shock are an order of magnitude larger than at the contact wave. This suggests that the 2-D pressure-based AI can be used to identify shock regions and to automatically distinguish them from other nonsmooth parts of the computed solution in the 2-D case as well.

TABLE IV. Explosion problem: The magnitude of the WLR computed at the final time $t^N = 3.2$.

Δx	$\max_{a^2 \le x^2_{j+\frac{1}{2}} + y^2_{k+\frac{1}{2}} \le b^2} \lvert E^{N-\frac{1}{2}}_{j+\frac{1}{2},k+\frac{1}{2}} \rvert$	Decay Rate	Δx	$\max_{a^2 \le x^2_{j+\frac{1}{2}} + y^2_{k+\frac{1}{2}} \le b^2} \lvert E^{N-\frac{1}{2}}_{j+\frac{1}{2},k+\frac{1}{2}} \rvert$	Decay Rate
Rarefaction edge, $a = 0$, $b = 0.35$			Contact wave, $a = 0.75$, $b = 1.15$		
3/200	2.036 e − 09	–	3/200	2.057 e − 08	–
3/400	1.362 e − 10	3.9	3/400	2.305 e − 09	3.2
3/800	3.865 e − 11	1.8	3/800	1.487 e − 10	4.0
3/1600	5.318 e − 12	2.9	3/1600	6.850 e − 11	1.1
3/3200	1.227 e − 12	2.1	3/3200	1.419 e − 11	2.3
Smooth subregion, $a = 0.3$, $b = 0.75$			Everywhere (Shock), $a = 0$, $b = 1$		
3/200	2.036 e − 09	–	3/200	8.645 e − 08	–
3/400	1.362 e − 10	3.9	3/400	2.183 e − 08	2.0
3/800	3.865 e − 11	1.8	3/800	5.362 e − 09	2.0
3/1600	5.318 e − 12	2.9	3/1600	1.320 e − 09	2.0
3/3200	1.227 e − 12	2.1	3/3200	3.302 e − 10	2.0

F. Two-Dimensional Numerical Experiments

Here, we demonstrate the performance of the proposed scheme adaption method on three examples taken from [43]. The "antidiffusion" coefficient $\alpha = 1$ is chosen in all of the 2-D experiments. The minmod parameter $\theta = 1.3$ is used in all of the 2-D experiments except for Example 7, where we take $\theta = 1.5$ to avoid excessive numerical diffusion in the computation. The adaption constant K is specified in each experiment.

CPU run times of our 2-D adaptive method have been about 10% longer than the corresponding CPU run times of a fully limited scheme.

Example 5 (Moving Contact Wave)**.** Similar to the 1-D Example 1, we will compare the performance of the high-order nonlimited and second-order limited schemes on an isolated contact wave. To build a suitable 2-D contact wave we consider a square computational domain $[0, 0.25] \times [0, 0.25]$ with nonreflecting boundary conditions and the following initial data:

$$\left(\overline{\rho}^0_{j,k}, u^0_{j,k}, v^0_{j,k}, p^0_{j,k}\right) = \begin{cases} (1.4, 0.2, 0.2, 1), & (x, y) \in D, \\ (1, 0.2, 0.2, 1), & \text{otherwise.} \end{cases}$$

The domain D is a rounded corner in the first quadrant, defined as the points satisfying both $x < 0.1$ and $y < 0.1$, as well as if the point is at the corner, $(x, y) \in [0.02, 0.1] \times [0.02, 0.1]$, then it must also be in the circle $C = \{(x, y) | (x - 0.02)^2 + (y - 0.02)^2 \le 0.08^2\}$.

We compute the solution until the final time $t = 0.25$ using both the high-order nonlimited and second-order fully limited schemes on the uniform grid with $\Delta x = \Delta y = 1/200$. As one can see in Fig. 6, the second-order solution (upper left) shows more deviation from the true solution (upper right)—visible as large patches of extreme color—near the contact than the high-order solution. One can also see that the high-order solution provides a sharper reproduction of the contact wave than the limited scheme, though it again exhibits oscillatory behavior (bottom row). Again the magnitude of oscillations is relatively small and stays under control as indicated by the experimental convergence rates, shown in Table V for the two schemes.

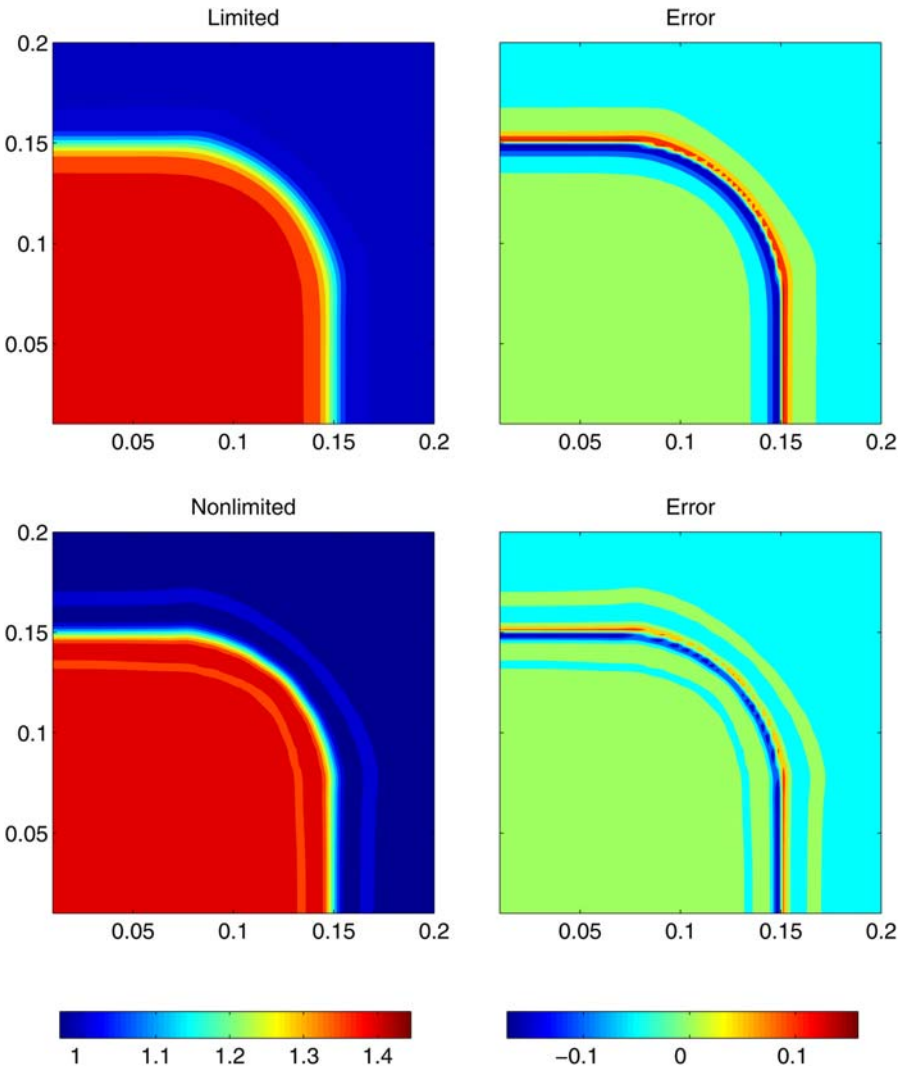

FIG. 6. Example 5: Density and errors computed by the second-order fully limited (top row) and high-order nonlimited (bottom row) schemes. [Color figure can be viewed in the online issue, which is available at wileyonlinelibrary.com.]

TABLE V. Example 5: L^1-errors and experimental convergence rates for the high-order nonlimited and second-order limited schemes.

$\Delta x = \Delta y$	(Nonlimited) $\|\|\rho^\Delta - \rho\|\|_1$	Rate	(Limited) $\|\|\rho^\Delta - \rho\|\|_1$	Rate
1/100	1.052 e − 03	–	1.419 e − 03	–
1/200	6.832 e − 04	0.62	8.990 e − 04	0.66
1/400	4.578 e − 04	0.58	5.939 e − 04	0.60
1/800	3.277 e − 04	0.48	4.122 e − 04	0.53
1/1600	2.578 e − 04	0.35	3.071 e − 04	0.42

Example 6 (Explosion)**.** This problem is taken from [42] (see also [32, 43], where different numerical schemes were tested on this problem). The initial data are radially symmetric and we set

$$(\overline{\rho}^0_{j,k}, u^0_{j,k}, v^0_{j,k}, p^0_{j,k}) = \begin{cases} (1,0,0,1), & x_j^2 + y_k^2 < 0.16, \\ (0.1,0,0,0.1), & \text{otherwise.} \end{cases}$$

Due to the symmetry of the problem, the computations are carried out in the domain $[0, 1.5] \times [0, 1.5]$ using the uniform grid with $\Delta x = \Delta y = 3/800$, reflecting boundary conditions at $x = 0$ and $y = 0$, and free boundary conditions at $x = 1.5$ and $y = 1.5$.

The density computed at time $t = 3.2$ by the fully limited second-order central-upwind scheme and by the proposed scheme adaption method with $K = 5$ are shown in Fig. 7. As it has been demonstrated in [32, 43], by $t = 3.2$ the circular contact curve typically develops instabilities (at smaller times, numerical diffusion present in nonoscillatory finite-volume schemes artificially stabilizes the contact curve). This example is a good test for the amount of numerical diffusion present in the studied schemes.

The density field, computed using a fully limited second-order scheme is presented in Fig. 7 (upper left). The contact wave becomes "curlier" when the mesh is refined (see Fig. 7 (upper right), where we have used the same fully limited scheme, but on a finer uniform grid with $\Delta x = \Delta y = 3/1600$). The contact wave computed by the scheme adaption method is even "curlier" though the coarser grid was used to obtain the solution shown in Fig. 7 (lower left). This can be explained by Fig. 7 (lower right), which demonstrates that the AI identifies the shock area almost exclusively so that the contact area is being treated by the nonlimited and thus much less diffusive high-order reconstruction (3.11).

Example 7 (Implosion)**.** In this example, we consider a square computational domain $[-0.3, 0.3] \times [-0.3, 0.3]$ with the solid wall boundary conditions and the following initial data:

$$(\rho, u, v, p)(x, y, 0) = \begin{cases} (0.125,0,0,0.14), & (x, y) \in D, \\ (1,0,0,1), & (x, y) \notin D, \end{cases}$$

where D is a diamond shape area with the vertices $(\pm 0.15, 0)$ and $(0, \pm 0.15)$.

Due to the symmetry of the problem, the computations are performed in the upper right quadrant only. For the fully limited scheme we present the solutions calculated on two uniform grids, one with $\Delta x = \Delta y = 3/4000$ and one at a finer resolution of $\Delta x = \Delta y = 3/8000$. The density computed at time $t = 2.5$ by the fully limited second-order central-upwind scheme and by the proposed scheme adaption method with $K = 150$ are shown in Fig. 8. As it has been shown in [43], a jet of liquid is expected to emerge. The numerical diffusion present in the second-order scheme will smear the jet out if the resolution of the grid is not fine enough, as shown in Fig. 8 (top row). This jet is clearly visible in the scheme adaption result (Fig. 8, lower left), which uses the lower resolution grid with $\Delta x = \Delta y = 3/4000$. In Fig. 8 (lower right), we plot the areas in which the second-order minmod reconstruction has been used by the adapted scheme. As one can see, the jet is being treated by the high-order nonlimited reconstruction (3.11) and the obtained result is thus very sharp.

Example 8 (Raleigh-Taylor Instability)**.** This problem is taken from [43]. Rayleigh-Taylor instability is a physical phenomenon appearing when a layer of heavier fluid is placed on top

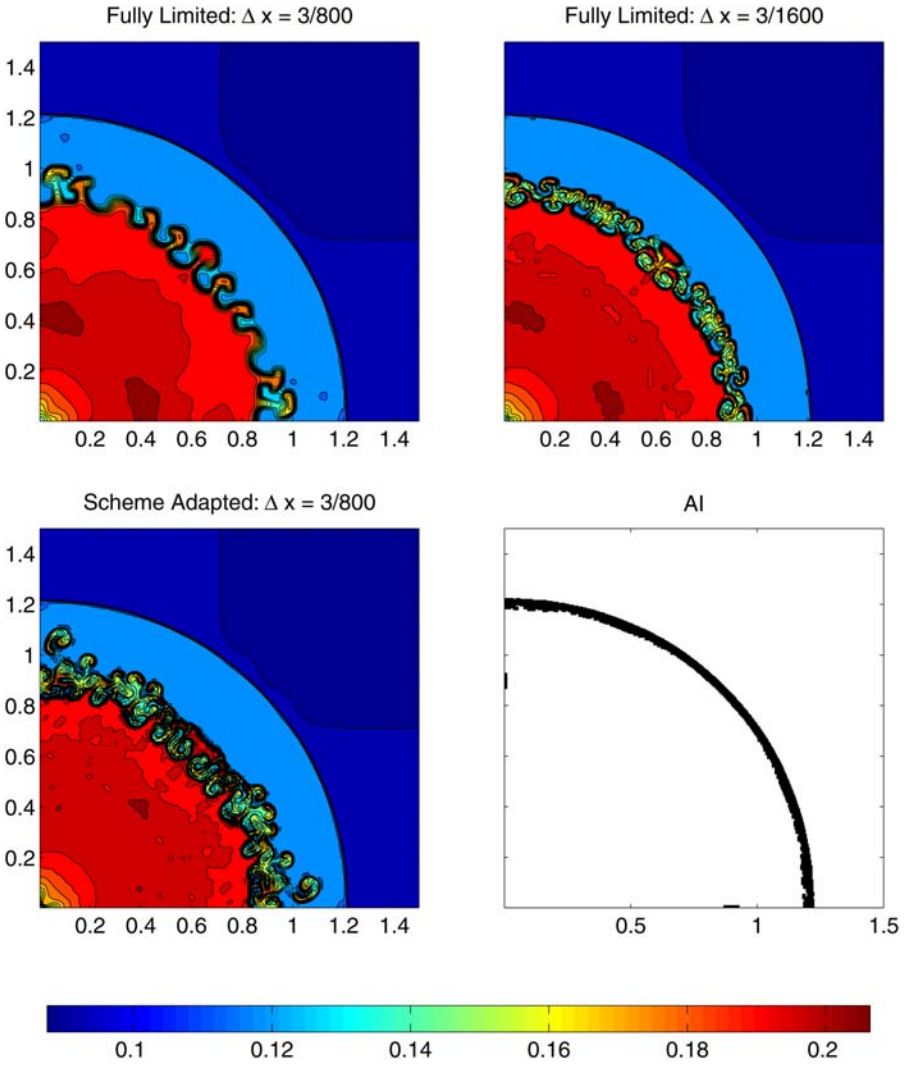

FIG. 7. Example 6: Density computed by the fully limited (top row) and adapted (lower left) schemes and the adaption areas (lower right). [Color figure can be viewed in the online issue, which is available at wileyonlinelibrary.com.]

of a layer of lighter fluid. To model such a situation, we include a gravitational source terms acting downward in the y-direction, that is, instead of (2.11), we solve the following 2-D system:

$$\begin{cases} \rho_t + (\rho u)_x + (\rho v)_y = 0, \\ (\rho u)_t + (\rho u^2 + p)_x + (\rho u v)_y = 0, \\ (\rho v)_t + (\rho u v)_x + (\rho v^2 + p)_y = -g\rho, \\ E_t + (u(E+p))_x + (v(E+p))_y = -g\rho v, \end{cases} \tag{4.2}$$

where g is a gravitational constant, taken as in the corresponding example in [43] to be $g = 0.1$.

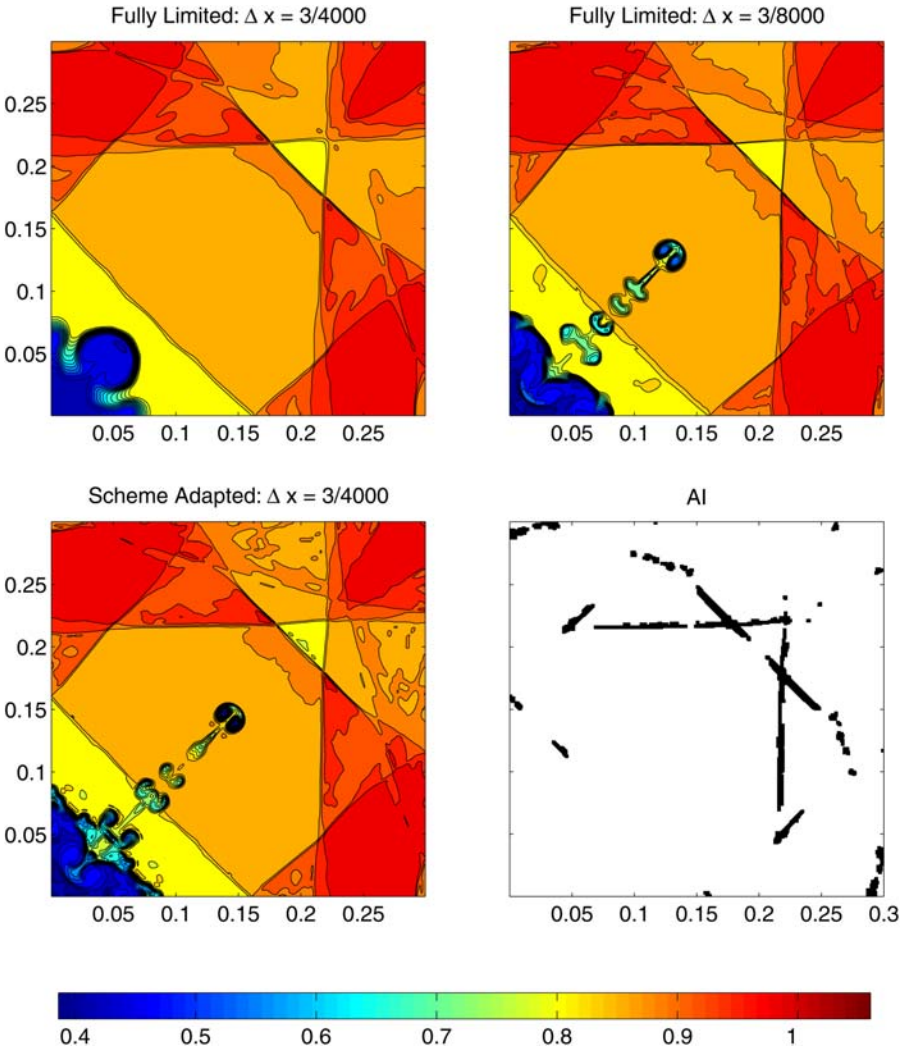

FIG. 8. Example 7: Density computed by the fully limited (top row) and adapted (lower left) schemes and the adaption areas (lower right). [Color figure can be viewed in the online issue, which is available at wileyonlinelibrary.com.]

We compute the solution of (4.2) in the domain $[-1/6, 1/6] \times [0, 1]$ and impose solid wall boundary conditions. The solution is evolved to $t = 8.5$. The initial value problem we consider is a heavy fluid of density 2 above a fluid of density 1 with the interface being a slightly perturbed line around $y = 0.5$, that is, we take the initial density to be

$$\rho(x, y, 0) = \begin{cases} 2, & y > y_{\text{int}}(x), \\ 1, & \text{otherwise}, \end{cases}$$

where

$$y_{\text{int}}(x) = 0.5 + 0.01\cos(6\pi x);$$

the initial pressure is set to be hydrostatic:

$$p(x, y, 0) = 0.1 + \begin{cases} 2g(1 - y), & y > y_{\text{int}}(x), \\ g(2 - y_{\text{int}}(x) - y), & \text{otherwise}, \end{cases}$$

and the fluids are assumed to be initially at rest: $u(x, y, 0) \equiv v(x, y, 0) \equiv 0$. To prevent turbulence caused by grid artifacts, we smooth ρ in the neighborhood of the interface by setting

$$\rho(x, y) = 1.5 + \frac{(y - y_{\text{int}}(x))}{4\Delta y}, \qquad \text{if } |y - y_{\text{int}}(x)| \le 2\Delta y.$$

This example is a useful one to test our method on, as the initial data has only a difference in the density—no strong shocks would develop if this were the homogeneous conservation law. However, this test problem includes gravity source terms which will cause the fluid to flow. Given this knowledge about the initial data, we would expect our AI to select only a very small part of the domain to be treated using the diffusive second-order reconstruction. In fact, since no strong shocks are developing in this example, the values of the WLR will be much more uniform than in the previous examples. We therefore take the adaption constant to be quite large. In Fig. 9, we compare three adaptive solutions to two fully limited solutions. The upper left 'Fully Limited' solution is computed with a fully limited scheme on a uniform grid with $\Delta x = 1/600$ and $\Delta y = 1/400$, where the 'Fine Resolution' solution was computed using $\Delta x = 1/1200$ and $\Delta y = 1/800$. The adaptive solutions are computed on the coarser grid with $\Delta x = 1/600$ and $\Delta y = 1/400$, but using the three different values of $K = 50$, 100 and 150. As expected, all of the adaptive solutions develop the Rayleigh-Taylor instabilities at the interface of the dense and light fluids, while a larger amount of the numerical diffusion present in the fully limited scheme artificially stabilizes the contact surface. With $K = 50$, which is still too small of a K value for this example, one can see appearance of some instabilities, but the numerical diffusion added in the areas where the nonlinear limiter has been applied does not allow finer structures to develop. With $K = 100$ and especially with $K = 150$, the limiter is (almost) not used and very fine turbulent structures can be observed along the entire interface.

Remark 4.2. To preserve a symmetry with respect to the y axis in Example 8, we have modified Step 1 in Algorithm 3.2 by setting

$$\begin{aligned} \boldsymbol{q}_{j+\frac{1}{2},k+\frac{1}{2}} &:= \frac{1}{4}\Big(\tilde{\boldsymbol{q}}(x_{j+\frac{1}{2}} - 0, y_{k+\frac{1}{2}} - 0) + \tilde{\boldsymbol{q}}(x_{j+\frac{1}{2}} - 0, y_{k+\frac{1}{2}} - 0) \\ &\quad + \tilde{\boldsymbol{q}}(x_{j+\frac{1}{2}} - 0, y_{k+\frac{1}{2}} - 0) + \tilde{\boldsymbol{q}}(x_{j+\frac{1}{2}} - 0, y_{k+\frac{1}{2}} - 0)\Big) \\ &= \frac{1}{720}[269(\overline{\boldsymbol{q}}_{j,k} + \overline{\boldsymbol{q}}_{j+1,k} + \overline{\boldsymbol{q}}_{j,k+1} + \overline{\boldsymbol{q}}_{j+1,k+1}) + 5(\overline{\boldsymbol{q}}_{j-1,k-1} + \overline{\boldsymbol{q}}_{j+2,k-1} + \overline{\boldsymbol{q}}_{j-1,k+2} + \overline{\boldsymbol{q}}_{j+2,k+2}) \\ &\quad - 53(\overline{\boldsymbol{q}}_{j-1,k} + \overline{\boldsymbol{q}}_{j,k-1} + \overline{\boldsymbol{q}}_{j+1,k-1} + \overline{\boldsymbol{q}}_{j+2,k} + \overline{\boldsymbol{q}}_{j-1,k+1} + \overline{\boldsymbol{q}}_{j,k+2} + \overline{\boldsymbol{q}}_{j+1,k+2} + \overline{\boldsymbol{q}}_{j+2,k+1}) \\ &\quad + 6(\overline{\boldsymbol{q}}_{j-2,k} + \overline{\boldsymbol{q}}_{j,k-2} + \overline{\boldsymbol{q}}_{j+1,k-2} + \overline{\boldsymbol{q}}_{j+3,k} + \overline{\boldsymbol{q}}_{j-2,k+1} + \overline{\boldsymbol{q}}_{j,k+3} + \overline{\boldsymbol{q}}_{j+1,k+3} + \overline{\boldsymbol{q}}_{j+3,k+1})] \end{aligned}$$

rather than $\boldsymbol{q}_{j+\frac{1}{2},k+\frac{1}{2}} := \boldsymbol{q}^{\text{NE}}_{j,k}$.

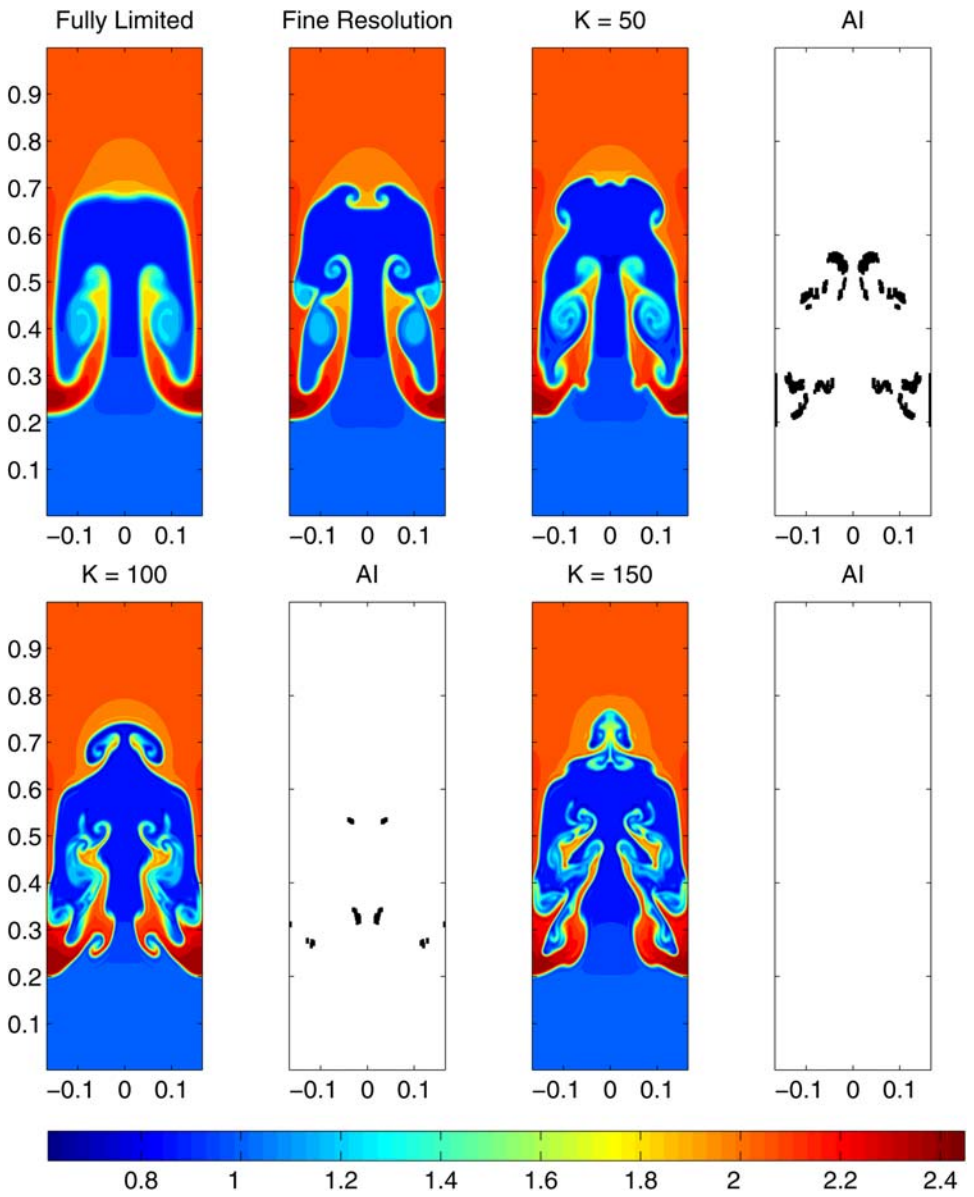

FIG. 9. Example 8: Density computed by the fully limited scheme on two uniform grids and three adapted schemes (with $K = 50$, 100 and 150) together with the corresponding adaption areas. [Color figure can be viewed in the online issue, which is available at wileyonlinelibrary.com.]

References

1. A. Harten, B. Engquist, S. Osher, and S. R. Chakravarthy, Uniformly high-order accurate essentially nonoscillatory schemes. III, J Comput Phys 71 (1987), 231–303.
2. R. J. LeVeque, Finite volume methods for hyperbolic problems, Cambridge Texts in Applied Mathematics, Cambridge University Press, Cambridge, 2002.

3. K.-A. Lie and S. Noelle, On the artificial compression method for second-order nonoscillatory central difference schemes for systems of conservation laws, SIAM J Sci Comput 24 (2003), 1157–1174.
4. H. Nessyahu and E. Tadmor, Nonoscillatory central differencing for hyperbolic conservation laws, J Comput Phys 87 (1990), 408–463.
5. P. K. Sweby, High resolution schemes using flux limiters for hyperbolic conservation laws, SIAM J Numer Anal 21 (1984), 995–1011.
6. B. van Leer, Towards the ultimate conservative difference scheme. V. A second-order sequel to Godunov's method, J Comput Phys 32 (1979), 101–136.
7. A. Kurganov and G. Petrova, A third-order semi-discrete genuinely multidimensional central scheme for hyperbolic conservation laws and related problems, Numer Math 88 (2001), 683–729.
8. S. Serna and A. Marquina, Power ENO methods: a fifth-order accurate weighted power ENO method, J Comput Phys 194 (2004), 632–658.
9. C.-W. Shu, High order weighted essentially nonoscillatory schemes for convection dominated problems, SIAM Rev 51 (2009), 82–126.
10. M. J. Berger and P. Colella, Local adaptive mesh refinement for shock hydrodynamics, J Comput Phys 82 (1989), 64–84.
11. M. J. Berger and J. Oliger, Adaptive mesh refinement for hyperbolic partial differential equations, J Comput Phys 53 (1984), 484–512.
12. K. G. Powell, P. L. Roe, and J. Quirk, Adaptive-mesh algorithms for computational fluid dynamics, Algorithmic trends in computational fluid dynamics (1991), ICASE/NASA LaRC Ser., Springer, New York, 1993, pp. 303–337.
13. J. J. Quirk, An adaptive mesh refinement algorithm for computational shock hydrodynamics, PhD Thesis, Cranfield Institute of Technology, UK, 1991.
14. J. J. Quirk, A parallel adaptive grid algorithm for computational shock hydrodynamics, Appl Numer Math 20 (1996), 427–453.
15. F. Aràndiga, A. Baeza, and R. Donat, Discrete multiresolution based on Hermite interpolation: computing derivatives, Commun Nonlinear Sci Numer Simul 9 (2004), pp. 263–273.
16. F. Aràndiga, A. Baeza, and R. Donat, Vector cell-average multiresolution based on Hermite interpolation, Adv Comput Math, 28 (2008), 1–22.
17. F. Aràndiga and R. Donat, Nonlinear multiscale decompositions: the approach of A. Harten, Numer Algorithms 23 (2000), 175–216.
18. F. Aràndiga, R. Donat, and A. Harten, Multiresolution based on weighted averages of the hat function. II. Nonlinear reconstruction techniques, SIAM J Sci Comput 20 (1999), 1053–1093 (electronic).
19. A. Gelb and E. Tadmor, Detection of edges in spectral data, Appl Comput Harmon Anal 7 (1999), 101–135.
20. A. Gelb and E. Tadmor, Detection of edges in spectral data. II. Nonlinear enhancement, SIAM J Numer Anal 38 (2000), 1389–1408 (electronic).
21. A. Gelb and E. Tadmor, Spectral reconstruction of piecewise smooth functions from their discrete data, M2AN Math Model Numer Anal 36 (2002), 155–175.
22. A. Gelb and E. Tadmor, Adaptive edge detectors for piecewise smooth data based on the minmod limiter, J Sci Comput 28 (2006), 279–306.
23. G. Puppo, Numerical entropy production for central schemes, SIAM J Sci Comput 25 (2003/04), 1382–1415 (electronic).
24. G. Puppo, The entropy regularity indicator for finite volume schemes, Hyperbolic problems: theory, numerics and applications. II, Yokohama Publ., Yokohama, 2006, pp. 235–242.
25. G. Puppo and M. Semplice, Numerical entropy and adaptivity for finite volume schemes, Commun Comput Phys, 10 (2011), 1132–1160.

26. J.-L. Guermond and R. Pasquetti, Entropy-based nonlinear viscosity for Fourier approximations of conservation laws, CR Math Acad Sci Paris 346 (2008), 801–806.

27. J.-L. Guermond, R. Pasquetti, and B. Popov, Entropy viscosity method for nonlinear conservation laws, J Comput Phys 230 (2011), 4248–4267.

28. S. Karni and A. Kurganov, Local error analysis for approximate solutions of hyperbolic conservation laws, Adv Comput Math 22 (2005), 79–99.

29. L. A. Constantin and A. Kurganov, Adaptive central-upwind schemes for hyperbolic systems of conservation laws, Hyperbolic problems: theory, numerics and applications. I, Yokohama Publ., Yokohama, 2006, pp. 95–103.

30. S. Karni, A. Kurganov, and G. Petrova, A smoothness indicator for adaptive algorithms for hyperbolic systems, J Comput Phys 178 (2002), 323–341.

31. R. Abgrall and S. Karni, A comment on the computation of non-conservative products, J Comput Phys 229 (2010), 2759–2763.

32. A. Kurganov and C.-T. Lin, On the reduction of numerical dissipation in central-upwind schemes, Commun Comput Phys 2 (2007), 141–163.

33. A. Kurganov, S. Noelle, and G. Petrova, Semi-discrete central-upwind scheme for hyperbolic conservation laws and Hamilton-Jacobi equations, SIAM J Sci Comput 23 (2001), 707–740.

34. A. Kurganov and E. Tadmor, New high resolution central schemes for nonlinear conservation laws and convection-diffusion equations, J Comput Phys 160 (2000), 241–282.

35. A. Kurganov and E. Tadmor, Solution of two-dimensional riemann problems for gas dynamics without riemann problem solvers, Numer Methods Partial Differential Equations 18 (2002), 584–608.

36. A. Kurganov and Y. Liu, New adaptive artificial viscosity method for hyperbolic systems of conservation laws, J Comput Phys 231 (2012), 8114–8132.

37. S. Gottlieb, D. Ketcheson, and C.-W. Shu, Strong stability preserving Runge-Kutta and multistep time discretizations, World Scientific, Hackensack, NJ, 2011.

38. S. Gottlieb, C.-W. Shu, and E. Tadmor, Strong stability-preserving high-order time discretization methods, SIAM Rev 43 (2001), 89–112.

39. X. Y. Hu, N. A. Adams, and C.-W. Shu, Positivity-preserving method for high-order conservative schemes solving compressible Euler equations, J Comput Phys 242 (2013), 169–180.

40. C.-W. Shu and S. Osher, Efficient implementation of essentially nonoscillatory shock-capturing schemes. II, J Comput Phys 83 (1989), 32–78.

41. P. Woodward and P. Colella, The numerical solution of two-dimensional fluid flow with strong shocks, J Comput Phys 54 (1988), 115–173.

42. E. F. Toro, Riemann solvers and numerical methods for fluid dynamics: A practical introduction, 3rd Ed., Springer-Verlag, Berlin, Heidelberg, 2009.

43. R. Liska and B. Wendroff, Comparison of several difference schemes on 1D and 2D test problems for the Euler equations, SIAM J Sci Comput 25 (2003), 995–1017.